A Novel Sensorless Predictive Voltage Control for an Induction Motor Drive Based on a Back-Stepping Observer-Experimental Validation

MAHMOUD A. MOSSA[ID][1]**, HAMDI ECHEIKH**[2]**, AND NGUYEN VU QUYNH**[ID][3]

[1]Electrical Engineering Department, Faculty of Engineering, Minia University, Minia 61111, Egypt
[2]Electrical Engineering Department, National Engineering School of Monastir, Monastir 5035, Tunisia
[3]Electrical and Electronics Department, Lac Hong University, Dong Nai 810000, Vietnam

Corresponding authors: Mahmoud A. Mossa (mahmoud_a_mossa@mu.edu.eg) and Nguyen Vu Quynh (vuquynh@lhu.edu.vn)

ABSTRACT The current paper presents a novel predictive voltage control (PVC) for an induction motor (IM) without using a speed sensor. The proposed PVC is formulated using the model predictive control principle in which the stator voltages are directly controlled rather than regulating the flux and torque as in traditional MP DTC. The advantages of the proposed PVC over the commonly used MP DTC scheme are the reduced calculation time, the reduced ripples and the fast dynamic. To realize the sensorless operation of the IM, a robust observer is used to estimate the speed, rotor flux, stator current and stator and rotor resistances. The observer is constructed based on the back-stepping theory. Testing the validness of the proposed sensorless PVC technique is performed in a form of comparison between the PVC and MP DTC procedures. The tests are firstly accomplished using the Matlab/Simulink software; then, a dSPACE 1104 test board is utilized for the experimental validation. The simulation and experimental results show that the IM dynamics are effectively enhanced when applying the proposed PVC in comparison with the MP DTC performance. The back-stepping observer (BSO) also proved its ability to estimate the specified variables for different operating speeds and under parameters variation as well.

INDEX TERMS Voltage control, IM, torque control, predictive control, sensorless control, BSO, cost function.

I. INTRODUCTION

Recently, the predictive control (PC) approach has been considered as an appropriate choice for obtaining better dynamics from induction motor (IM) drives [1]–[6]. The PC approach has different formulations which are categorized based on the cost function's form. As an illustration, in [1], [2], the MP DTC was considered, in which the error minimization equation consisted of the torque and flux errors, besides using a weighting value for moderating the effect of the two variables on each other. In [3], [4], the predictive current control (PCC) was considered, in which the error function consisted of two similar parts of the stator current alfa-beta (α-β) or direct-quadrature (d-q) components. In [5], [6], the authors proposed an error function form which consisted of the flux components, and thus the weighting

The associate editor coordinating the review of this manuscript and approving it for publication was Huiqing Wen[ID].

value was omitted, which simplified the cost function and reduced the calculation time taken by the controller. The drawback of this topology is that the precise estimation of the flux components must be ensured for all operating cases, and to fulfill this need, adaptive flux observers must be incorporated which adds extra burden to the computation time.

The predictive control replaced the operation of the classic DTC and FOC control approaches due to many reasons [7]–[9]. For example, the system's complexity is reduced through eliminating the look-up tables and hysteresis regulators used in DTC, and eliminating the PI current controllers used in the FOC. Moreover, the ripples in the controlled signals are effectively suppressed when adopting the MP DTC compared with the DTC and FOC.

However the IM dynamics are improved through applying the predictive control with its different forms, but the control systems are still having some deficiencies which need to be avoided. For example; in the PCC approach, the cost function

depends on the estimated currents at instant $(K+1)T_s$, and thus it depends directly on the precision of the current measurement, which can be affected by the noise [2], [10]–[12]. Moreover, the prediction model itself is depending on the machine parameters which can be changed under certain conditions (i.e. the flux and speed estimation at low frequencies).

In MP DTC, the error minimization function uses a weighting value; so there is a vital need for the precise and correct selection of this value, which in turn requires using an online optimization procedure which adds extra calculation time [13]–[15]. Moreover, the ripples are still present in the controlled variables; however its percentage is lower than that of classic DTC. This can be referred to many reasons; one of them is the wrong choice of the weighting value. Another reason is referred to the voltage implementation for the total sampling period, which is not a precise control action, as it may happens that there is a need to update the voltage vector within the sampling interval itself, which finally results in increasing the flux and torque deviations and thus the ripples increase again. Other studies have concerned with limiting the ripples in the MP DTC through incorporating adaptive flux estimators in the system [16], [17], which improved the flux and torque estimations, but on the other hand it added a delay in the response and increased the system complexity.

Different studies were introduced to avoid using a weighting value through utilizing a cost function of similar terms [5], [18]. The performance was significantly improved using these techniques; however the cost functions in these studies used parameters dependent variables such as the flux [5], [6], which made the controller very sensitive to the parameters variation. In model predictive flux (MPF) schemes, the flux error was used as the cost function's element which needs to be minimized. The main challenge in these procedures is how to ensure the precise estimation of stator flux, which inherently depends on the system parameters. Moreover, the cost function terms are still needed to be calculated and predicted which means that the computation burden is not yet completely minimized even it is lower than the computational burden of the MP DTC.

To enhance the reliability and robustness of the drive, different speed estimation procedures were proposed [19]–[22]. Some of them depended on utilizing extended Luenberger estimator, neural network estimator, extended Kalman filter and least squared error technique as well. The main deficiency of such observers is the system complexity which requires high computation needs that cannot be afforded by all microprocessors. The model reference adapting observer (MRAO) is extensively used for the speed estimation purpose [23]–[25]. However, the MRAO is very attentive to any variation in the parameters particularly at low operating frequencies which requires the precise determination of the motor model at all operating conditions. A deterministic Luenberger observer has been proposed in [26], which investigated and tested the observer's response to the parameters mismatch, but on the other hand it ignored testing the system's robustness against the measurement accuracy.

In order to solve some of the deficiencies in the traditional MP DTC, and to ensure a robust performance from the speed estimator, the current work introduces a novel sensorless predictive voltage control (PVC) approach. The advantages of the proposed procedure are the simplicity, the fast dynamic change, the reduced ripples and low computation time. These merits are obtained through using a simple error function form with terms of the same category (d-q stator voltages). Moreover, the used variables in this function are not estimated one which enhances the system robustness. Furthermore, as the stator voltages are the nearest variables to be applied to the IM; this contributes in fastening the dynamic response of the IM.

To ensure high system reliability and reducing the cost, a robust BSO observer is used for observing the stator current, the rotor flux, the rotor speed and stator and rotor resistances as well. The structure of the observer is very simple compared with the other techniques. The BSO provides a precise estimation of different variables in a cascaded manner which significantly contributes in limiting the estimation error. The BSO has been used with different AC machines as a control scheme [27]–[30], but it is unfamiliary utilized as an observer.

Up to this review, the current paper concerns with introducing some contributions which can be addressed as following;

- The paper introduces a novel PVC for an IM drive.
- The proposed PVC is designed and explained in details.
- The PVC has the advantages of simplicity, robustness and fast dynamic response compared with traditional predictive controllers such as MP DTC approach.
- A robust BSO is designed and used to estimate different variables and parameters.
- The robustness of the proposed sensorless PVC approach is tested for different dynamic operations and under system uncertainties as well.
- Comprehensive tests are executed to check the feasibility of the designed controller. Using these results, a comparison is made between the novel PVC and MP DTC techniques.

The present study is structured such that: In Sec II, the IM equivalent model is described. In Sec III, the proposed PVC is introduced and explained. After that, the proposed BSO observer is designed and described in Sec IV. In Sec V, the complete system layout is described. In Secs VI, VII, the test results are introduced and discussed for the two procedures (MP DTC and proposed PVC). The last section (Sec VIII) is concerned with introducing the research outcomes and the conclusion.

II. EQUIVALENT CIRCUIT OF IM

The IM circuit model can be configured as shown in Figure 1, where all variables are identified in a frame which is rotating with the same frequency of rotor flux vector $\omega_{\bar{\psi}_r}$.

In Fig. 1, the symbols R_s and R_r pertain to the resistances of stator and rotor windings. While the leakage inductances are expressed by L_{ls} and L_{lr}, respectively. The magnetizing inductance is also expressed by L_m. The rotor angular
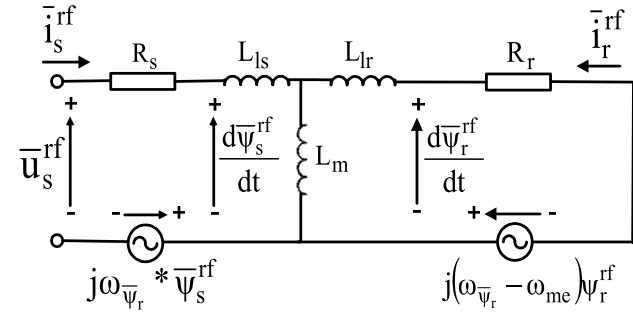
FIGURE 1. Model of IM.

frequency is represented by $\omega_{me} = p\omega_m$, where p is the pole pairs and ω_m is the mechanical speed. The superscript 'rf' reports that all variables are represented in a frame which is synchronized with the rotor flux vector. The stator voltage, stator current and stator flux vectors are represented by $\bar{u}_s^{rf}$, $\bar{i}_s^{rf}$ and $\bar{\psi}_s^{rf}$, consecutively. While the rotor flux and current vectors are defined by $\bar{\psi}_r^{rf}$ and $\bar{i}_r^{rf}$, respectively.

Using the model in Fig. 1, the electric dynamics of IM can be described by the following expressions

$$\frac{d\bar{\psi}_{s,k}^{rf}}{dt} = \bar{u}_{s,k}^{rf} - R_s\bar{i}_{s,k}^{rf} - j\omega_{\bar{\psi}_r}\bar{\psi}_{s,k}^{rf} \tag{1}$$

$$\frac{d\bar{\psi}_{r,k}^{rf}}{dt} = -R_r\bar{i}_{r,k}^{rf} - j\left(\overbrace{\omega_{\bar{\psi}_{r,k}} - \omega_{me,k}}^{\omega_{slip,k}}\right)\bar{\psi}_{r,k}^{rf} \tag{2}$$

$$\frac{d\omega_{me,k}}{dt} = \frac{p}{J}\left(T_{e,k} - T_{l,k}\right) \tag{3}$$

where, $T_{e,k}$ and $T_{l,k}$ are the motor and load torques, respectively. J is referring to the motor's inertia.

The motor's torque $T_{e,k}$ can be evaluated using the cross product of the fluxes by

$$T_{e,k} = 1.5p\frac{L_m}{\sigma L_s L_r}\bar{\psi}_{s,k} \times \bar{\psi}_{r,k} \tag{4}$$

where $\sigma = 1 - \left(L_m^2/L_s L_r\right)$ is the total leakage factor.

The flux vectors in (4) can be represented exponentialy as follows,

$$\bar{\psi}_{s,k} = \left|\bar{\psi}_{s,k}\right| e^{j\omega_{\bar{\psi}_{s,k}}t}, \text{ and } \bar{\psi}_{r,k} = \left|\bar{\psi}_{r,k}\right| e^{j\omega_{\bar{\psi}_{r,k}}t} \tag{5}$$

where $\omega_{\bar{\psi}_{s,k}}$ and $\omega_{\bar{\psi}_{r,k}}$ are the angular frequencies of the stator and rotor fluxes, accordingly.

The expression in (4) will be used later to design the PI torque controller which is used to develop the reference voltage $u_{qs,k}^*$. Meanwhile, the first equality in (5) will be utilized to design the PI flux controller which is used to develop the reference voltage $u_{ds,k}^*$. After that, both $u_{ds,k}^*$ and $u_{qs,k}^*$ are used in the proposed cost function of the controller as illustrated in the next section.

III. PROPOSED PVC APPROACH
The operation mechanism of the designed PVC approach is articulated on using an error minimization function which includes two similar terms. These terms are the

absolute errors between the actual and reference quantities of the stator voltage d-q terms. The actual terms ($u_{ds,k+1}$ and $u_{qs,k+1}$) are procured from the output of the controllers using the switching states, while the reference d-q voltages ($u_{ds,k+1}^*$ and $u_{qs,k+1}^*$) are calculated using the designed two regulators. The inputs of the adaptors are the torque and stator flux errors. The design of the two regulators is performed as follows,

A. DESIGN OF STATOR FLUX REGULATOR
As mentioned earlier, that the stator flux regulator is utilized to get the reference voltage $u_{ds,k+1}^*$, and to ensure the correct operation, the transfer function of the flux regulator must be correctly determined.

From (5), the stator flux vector is represented in the stator frame $"s"$ at time $(k + 1)T_s$ by

$$\bar{\psi}_{s,k+1}^s = \left|\bar{\psi}_{s,k+1}^s\right| e^{j\omega_{\bar{\psi}_{s,k+1}}t} = \left|\bar{\psi}_{s,k+1}^s\right| e^{j\theta_{s,k+1}} \tag{6}$$

Afterwards,

$$\left|\bar{\psi}_{s,k+1}^s\right| = \bar{\psi}_{s,k+1}^s e^{-j\theta_{s,k+1}}$$
$$= \bar{\psi}_{s,k+1}^s\left(\cos\theta_{s,k+1} - j\sin\theta_{s,k+1}\right) \tag{7}$$

Taking the Laplace transform of (7), then

$$\left|\bar{\psi}_{s,k+1}^s\right|(s) = \bar{\psi}_{s,k+1}^s(s) * \left[\frac{s}{s^2 + \theta_{s,k+1}^2} - j\frac{\theta_{s,k+1}}{s^2 + \theta_{s,k+1}^2}\right] \tag{8}$$

And,

$$\theta_{s,k+1} = \omega_{\bar{\psi}_{s,k+1}}t = \omega_{\bar{\psi}_{s,k+1}}T_s \cong 0.0 \tag{9}$$

where T_s is the sampling time.

Then,

$$\left|\bar{\psi}_{s,k+1}^s\right|(s) = \bar{\psi}_{s,k+1}^s(s) * \frac{1}{s} \tag{10}$$

Furthermore, the stator flux can be expressed in frequency domain (s) under field orientation as follows

$$\bar{\psi}_{s,k+1}^{rf}(s) = \psi_{ds,k+1}^{rf}(s) + j\psi_{qs,k+1}^{rf}(s) \tag{11}$$

By replacing (11) into (10) represented in synchronous frame, this results in

$$\left|\bar{\psi}_{s,k+1}^{rf}\right|(s) = \bar{\psi}_{s,k+1}^{rf}(s) * \frac{1}{s}$$
$$= \left[\psi_{ds,k+1}^{rf}(s) + j\psi_{qs,k+1}^{rf}(s)\right] * \frac{1}{s} \tag{12}$$

Then, from (11) and (12)

$$\left|\bar{\psi}_{s,k+1}^{rf}\right|(s) = \psi_{ds,k+1}^{rf}(s) * \frac{1}{s} \text{ \& } j\psi_{qs,k+1}^{rf}(s) * \frac{1}{s} = 0.0 \tag{13}$$

From (1), the value of $\psi_{ds,k+1}^{rf}(s)$ can be expressed in another form by

$$\psi_{ds,k+1}^{rf}(s) = \left(u_{ds,k+1}^{rf}(s) - R_s i_{ds,k+1}^{rf}(s)\right)T_s$$
$$= \left(u_{ds,k+1}^{rf}(s) - R_s\frac{\psi_{dr,k+1}^{rf}(s)}{L_m}\right)T_s \tag{14}$$

where $i^{rf}_{ds,k+1} = \psi^{rf}_{dr,k+1}/L_m$ under rotor field orientation (RFO).

The quantity $R_s \frac{\psi^{rf}_{dr,k+1}(s)}{L_m} T_s \cong 0.0$ is very small and can be neglected. Then,

$$\widetilde{\psi^{rf}_{ds,k+1}}(s) = \frac{\widetilde{u^{rf}_{ds,k+1}}(s)}{s} * T_s \quad (15)$$

From (15), it is very obvious that the flux is managed through controlling the voltage $u^{rf}_{ds,k+1}$. Then, from (15), the transfer function which is used to tune the flux regulator is expressed by

$$\frac{\psi^{rf}_{ds,k+1}(s)}{u^{rf}_{ds,k+1}(s)} = \frac{T_s}{s} \quad (16)$$

B. DESIGN OF TORQUE REGULATOR

Using (2), and after some calculations, the relationships which relates the rotor and stator flux dynamics can be written by

$$\frac{d\bar{\psi}^{rf}_{r,k+1}}{dt} = \frac{L_m R_r}{\sigma L_s L_r}\bar{\psi}^{rf}_{s,k+1} - \left(j\omega_{slip,k+1} + \frac{R_r}{\sigma L_r}\right)\bar{\psi}^{rf}_{r,k+1} \quad (17)$$

Applying Laplace transform on (17), it results

$$\bar{\psi}^{rf}_{r,k+1}(s) = \frac{(L_m/L_s)}{s\left(\sigma\frac{L_r}{R_r}\right) + \left(1 + j\omega_{slip,k+1}\frac{\sigma L_r}{R_r}\right)}\bar{\psi}^{rf}_{s,k+1}(s) \quad (18)$$

By substituting the value of $\bar{\psi}^{sf}_{s,k+1}(s)$ from (10) into (18), it results

$$\bar{\psi}^{rf}_{r,k+1}(s) = \frac{(L_m/L_s)\,s}{s\left(\sigma\frac{L_r}{R_r}\right) + \left(1 + j\omega_{slip,k+1}\frac{\sigma L_r}{R_r}\right)}\left|\bar{\psi}^{rf}_{s,k+1}\right|(s) \quad (19)$$

Now, by substituting from (10) and (19) into (4), the torque expression in frequency domain can be represented by

$$T_{e,k+1}(s) = 1.5p\frac{L_m s}{\sigma L_s L_r}\left|\bar{\psi}^{rf}_{s,k+1}\right|(s)$$
$$\times \frac{(L_m/L_s)\,s}{s\left(\sigma\frac{L_r}{R_r}\right) + \left(1 + j\omega_{slip,k+1}\frac{\sigma L_r}{R_r}\right)}\left|\bar{\psi}^{rf}_{s,k+1}\right|(s) \quad (20)$$

where $\left|\bar{\psi}^{rf}_{s,k+1}\right|$ is the stator flux amplitude which is assumed to be fixed. Then, the Laplace inverse of (20) gives the torque expression in terms of the slip frequency $\omega_{slip,k}$ as

$$T_{e,k+1} = \left[1.5p\frac{L_m^2}{R_r L_s^2}\left|\bar{\psi}^{rf}_{s,k+1}\right|^2\right]\left(1 - e^{\frac{-t}{T_f}}\right)\omega_{slip,k+1} \quad (21)$$

where $T_f = \sigma\frac{L_r}{R_r}$ is the time shift between the stator and rotor flux vectors.

The slip speed $\omega_{slip,k+1}$ under rotor field orientation is expressed by

$$\omega_{slip,k+1} = \frac{L_m i^{rf}_{qs,k+1}}{T_r\left|\bar{\psi}^{rf}_{r,k+1}\right|} = \frac{L_m L_s i^{rf}_{qs,k+1}}{L_s T_r\left|\bar{\psi}^{rf}_{r,k+1}\right|}$$
$$= \frac{L_m \psi^{rf}_{qs,k+1}}{\sigma L_s T_r\left|\bar{\psi}^{rf}_{r,k+1}\right|} \quad (22)$$

where $T_r = L_r/R_r$ is the rotor's constant.

Then by replacing the value of (22) into (21), it results

$$T_{e,k+1} = \left[1.5p\frac{L_m^2}{\sigma T_r R_r L_s^2}\frac{\left|\bar{\psi}^{rf}_{s,k+1}\right|^2}{\left|\bar{\psi}^{rf}_{r,k+1}\right|}\right]\left(1 - e^{\frac{-t}{T_f}}\right)\psi^{rf}_{qs,k+1} \quad (23)$$

From (23), it is realized that the torque can be regulated via managing the flux $\psi^{rf}_{qs,k+1}$.

From (1), and by neglecting the resistance voltage drop $R_s i^{rf}_{qs,k+1}$, and assuming steady state operation, the value of $\psi^{rf}_{qs,k+1}$ can be calculated as follows

$$\psi^{rf}_{qs,k+1} = \int\left(u^{rf}_{qs,k+1} - \overbrace{\frac{d\psi^{rf}_{qs,k+1}}{dt}}^{\cong 0.0} - \overbrace{R_s i^{rf}_{qs,k+1}}^{\cong 0.0}\right)dt$$
$$= u^{rf}_{qs,k+1}T_s \quad (24)$$

From (24), it is very obvious that the flux q-component is managed by the voltage component $u^{rf}_{qs,k+1}$, and consequently the torque $T_{e,k+1}$ can be regulated using $u^{rf}_{qs,k+1}$.

Using (24) and by replacing into (23), it becomes

$$\widetilde{T_{e,k+1}} = \left[1.5p\frac{L_m^2 T_s}{\sigma T_r R_r L_s^2}\frac{\left|\bar{\psi}^{rf}_{s,k+1}\right|^2}{\left|\bar{\psi}^{rf}_{r,k+1}\right|}\right]\left(1 - e^{\frac{-t}{T_f}}\right)\widetilde{u^{rf}_{qs,k+1}} \quad (25)$$

By taking the Laplace transform of (25), the transfer function of the torque controller can be written by

$$\frac{T_{e,k+1}(s)}{u^{rf}_{qs,k+1}(s)} = \frac{\left[1.5p\frac{L_m^2 T_s}{\sigma T_r R_r L_s^2}\frac{\left|\bar{\psi}^{rf}_{s,k+1}\right|^2}{\left|\bar{\psi}^{rf}_{r,k1+}\right|}\right]}{T_f s + 1} \quad (26)$$

Now, (26) can be used to tune the coefficients of the torque regulator.

After tuning the flux and torque regulators using (16) and (26), the reference voltages $u^*_{ds,k+1}$ and $u^*_{qs,k+1}$ can be obtained and then used in the following error function form,

$$\tilde{\xi}^i_{k+1} = \left|u^*_{ds,k+1} - u_{ds,k+1}\right|^i + \left|u^*_{qs,k+1} - u_{qs,k+1}\right|^i \quad (27)$$

From (27), it is concluded that the designed cost function is simpler in construction than the function used by many topologies of MP DTC approach [15], [16], and which is expressed as following

$$\tilde{\Delta}_{k+1}^i = \left| T_{e,k+1}^* - \tilde{T}_{e,k+1} \right|^i + w_f \left| \psi_{s,k+1}^* - \tilde{\tilde{\psi}}_{s,k+1} \right|^i \quad (28)$$

Via comparing (27) and (28), it is found that (27) does not contain any estimated variables as (28), and it doesn't utilize a weighting value as well, which makes (27) very robust against the problems of imprecise estimation.

Concerning the feedback voltage signals $(u_{ds,k+1}, u_{qs,k+1})$ to be used in (27), and used also as an input to the BSO as illustrated in Fig. 3 and to avoid the utilization of the PWM pulse signal, the finite control set (FCS) mechanism is adopted. The FCS enables the calculation of the voltages using a definite vectors set (eight vectors), where each vector is corresponding to specified switching states. Therefore, the switching states are determined firstly and then the voltages are extraxted according to the following code:

```
Function [u_ds^buffered, u_qs^buffered]= fcn (u*_ds, u*_qs, u_ds, u_qs);
 persistent s_opt
  if isempty (s_opt),
    s_opt = 1;
  end
u_0 = 0;
u_1 = 2/3*U_dc;
            ⋮
u_7 = 0;
u = [u_0 u_1 u_2 u_3 u_4 u_5 u_6 u_7];
states = [0 0 0;1 0 0;1 1 0;0 1 0;0 1 1;0 0 1;1 0 1;1 1 1];
  ζ_opt = 1e^10;
   for i = 1:8
   u_ds(i) =real (u(i)); u_qs(i) =imag (u(i));
   ζ = abs(u*_ds-u_ds(i))+ abs(u*_qs - u_qs(i));
 if (ζ < ζ_opt)
  ζ_opt = ζ;   s_opt = i;
    end
  end
[∼, s_opt] = min(ζ);
%%%  Determination of states
S_a = states(s_opt,1);
S_b = states(s_opt,2);
S_c = states(s_opt,3);
%%%  controller's output voltages
u_as = U_dc/3 (2S_a − S_b − S_c);
u_bs = U_dc/3 (2S_b − S_a − S_c);
u_cs = U_dc/3 (2S_c − S_b − S_a);
u_αs = 2/3 (u_as − 1/2 u_bs − 1/2 u_cs); u_βs = 2/3 (0 + √3/2 u_bs − √3/2 u_cs);
u_ds = u_αs cos θ_ψ̄r,k + u_βs sin θ_ψ̄r,k;   ⎱ → Voltages to be used
u_qs = −u_αs sin θ_ψ̄r,k + u_βs cos θ_ψ̄r,k;   ⎰     by the controller
```

IV. BACK-STEPPING OBSERVER (BSO)
The Lyapunov theory is used to design the the back-stepping approach. This technique is commonly adopted when designing the control formulas for nonlinear systems. Most of the
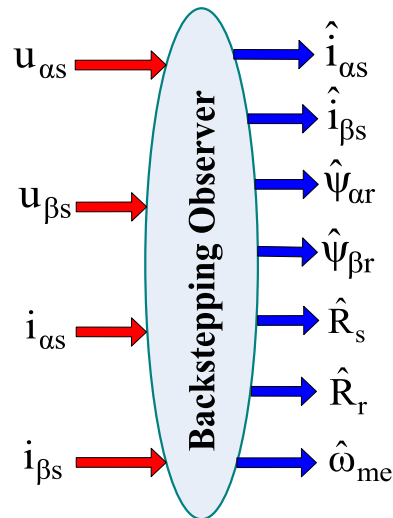
FIGURE 2. Inputs/Outputs of proposed BSO.

used state observers for IM which articulated on the back-stepping principle were used for observing the inductive and resistive quantities of the motor while using mechanical sensor. Despite that, the challenge appears when removing the sensor due to the deterioration of observability specifically at low operating frequencies. For example, the used technique in [31] should be adapted to consider the system's nonlinearity by providing extra damping parts for each input of the control. In the proposed BSO, the input nonlinearities to the subsystems are admitted to be a function of the subsystem's output and the upper subsystem's states, along with the immeasurable variables. The inputs of the BSO are the stator voltages and currents, meanwhile the outputs are the observed currents, rotor flux, speed, and stator and rotor resistances.

Estimating the speed and rotor resistance in the same time is a very difficult process especially in steady state operation [32], and this can be inferred to the inherited coupling between the estimation errors of the speed and resistance. This fact can be easily realized via checking the equivalent circuit of IM in Fig. 1. So, as a solution for this issue, two cascaded BSOs with the same parameters are used to firstly observe the speed and then the observed speed is utilized to estimate the rotor resistance. The predictive control system basically determines its calculation capacity based on the time taken to compute the cost function, so the main influence term in the execution time is that time taken in each cycle to evaluate the convergence condition terms and not any other unit in the control system.

A. DESIGN OF BSO
The stator current is a measured variable and it is considered as output from the observer. The current components are then expressed by

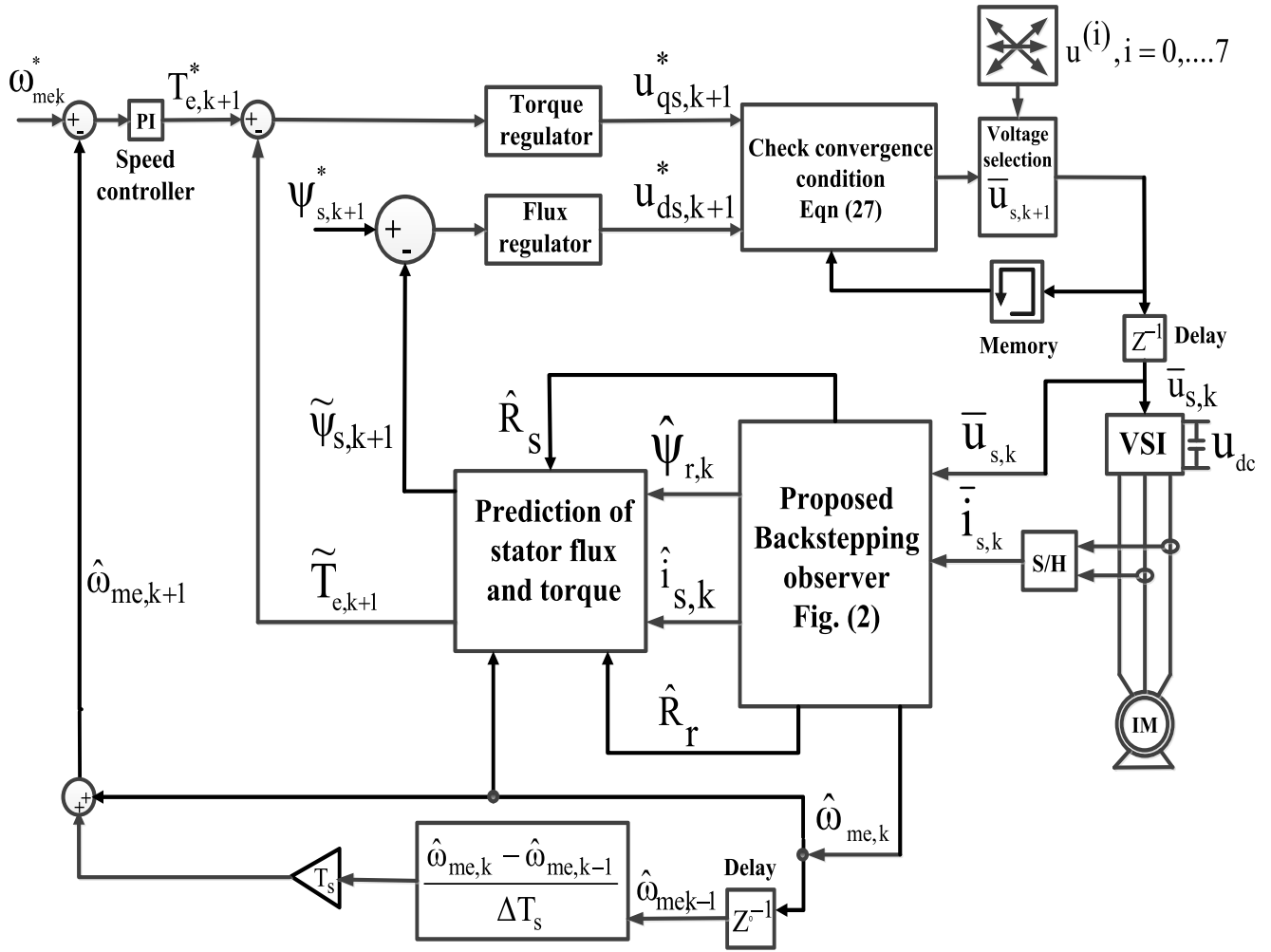$$h_\alpha = i_{\alpha s}, h_\beta = i_{\beta s} \quad (29)$$

FIGURE 3. Proposed sensorless PVC approach for IM drive.

The BSO can be modeled using the following relationships

$$\frac{d\hat{\psi}_{\alpha r}}{dt} = -\frac{\hat{R}_r}{L_r}\hat{\psi}_{\alpha r} - \hat{\omega}_{me}\hat{\psi}_{\beta r} + \frac{\hat{R}_r L_m}{L_r}h_\alpha$$

$$\frac{d\hat{\psi}_{\beta r}}{dt} = -\frac{\hat{R}_r}{L_r}\hat{\psi}_{\beta r} + \hat{\omega}_{me}\hat{\psi}_{\alpha r} + \frac{\hat{R}_r L_m}{L_r}h_\beta$$

$$\frac{d\hat{i}_{\alpha s}}{dt} = \frac{\hat{R}_r L_m}{\sigma L_s L_r^2}\hat{\psi}_{\alpha r} + \frac{L_m}{\sigma L_s L_r}\hat{\omega}_{me}\hat{\psi}_{\beta r}$$
$$- \frac{L_m^2\hat{R}_r + L_r^2\hat{R}_s}{\sigma L_s L_r^2}h_\alpha + \frac{1}{\sigma L_s}u_{\alpha s} + s_\alpha$$

$$\frac{d\hat{i}_{\beta s}}{dt} = \frac{\hat{R}_r L_m}{\sigma L_s L_r^2}\hat{\psi}_{\beta r} - \frac{L_m}{\sigma L_s L_r}\hat{\omega}_{me}\hat{\psi}_{\alpha r}$$
$$- \frac{L_m^2\hat{R}_r + L_r^2\hat{R}_s}{\sigma L_s L_r^2}h_\beta + \frac{1}{\sigma L_s}u_{\beta s} + s_\beta \quad (30)$$

where s_α and s_β are the inputs of the control which will be designed using the back-stepping technique.

From (30), the estimation errors can be described by

$$\frac{d\tilde{\psi}_{\alpha r}}{dt} = -\frac{\tilde{R}_r}{L_r}\psi_{\alpha r} - \frac{\hat{R}_r}{L_r}\tilde{\psi}_{\alpha r} - \hat{\omega}_{me}\tilde{\psi}_{\beta r} - \tilde{\omega}_{me}\psi_{\beta r} + \frac{\tilde{R}_r L_m}{L_r}h_\alpha$$

$$\frac{d\tilde{\psi}_{\beta r}}{dt} = -\frac{\tilde{R}_r}{L_r}\psi_{\beta r} - \frac{\hat{R}_r}{L_r}\tilde{\psi}_{\beta r} + \hat{\omega}_{me}\tilde{\psi}_{\alpha r} + \tilde{\omega}_{me}\psi_{\alpha r} + \frac{\tilde{R}_r L_m}{L_r}h_\beta$$

$$\frac{d\tilde{i}_{\alpha s}}{dt} = \frac{\tilde{R}_r L_m}{\sigma L_s L_r^2}\psi_{\alpha r} + \frac{\hat{R}_r L_m}{\sigma L_s L_r^2}\tilde{\psi}_{\alpha r} + \frac{L_m}{\sigma L_s L_r}\hat{\omega}_{me}\tilde{\psi}_{\beta r}$$
$$+ \frac{L_m}{\sigma L_s L_r}\tilde{\omega}_{me}\psi_{\beta r} - \frac{L_m^2\tilde{R}_r + L_r^2\tilde{R}_s}{\sigma L_s L_r^2}h_\alpha + s_\alpha$$

$$\frac{d\tilde{i}_{\beta s}}{dt} = \frac{\tilde{R}_r L_m}{\sigma L_s L_r^2}\psi_{\beta r} + \frac{\hat{R}_r L_m}{\sigma L_s L_r^2}\tilde{\psi}_{\beta r} - \frac{L_m}{\sigma L_s L_r}\hat{\omega}_{me}\tilde{\psi}_{\alpha r}$$
$$- \frac{L_m}{\sigma L_s L_r}\tilde{\omega}_{me}\psi_{\alpha r} - \frac{L_m^2\tilde{R}_r + L_r^2\tilde{R}_s}{\sigma L_s L_r^2}h_\beta + s_\beta$$

$$\tilde{h}_\alpha = \tilde{i}_{\alpha s}$$
$$\tilde{h}_\beta = \tilde{i}_{\beta s} \quad (31)$$

where $\tilde{\psi}_{\alpha r} = \hat{\psi}_{\alpha r} - \psi_{\alpha r}$, $\tilde{\psi}_{\beta r} = \hat{\psi}_{\beta r} - \psi_{\beta r}$, $\tilde{i}_{\alpha s} = \hat{i}_{\alpha s} - i_{\alpha s}$, $\tilde{i}_{\beta s} = \hat{i}_{\beta s} - i_{\beta s}$, $\tilde{R}_s = \hat{R}_s - R_s$, $\tilde{R}_r = \hat{R}_r - R_r$, $\tilde{\omega}_{me} = \hat{\omega}_{me} - \omega_{me}$.
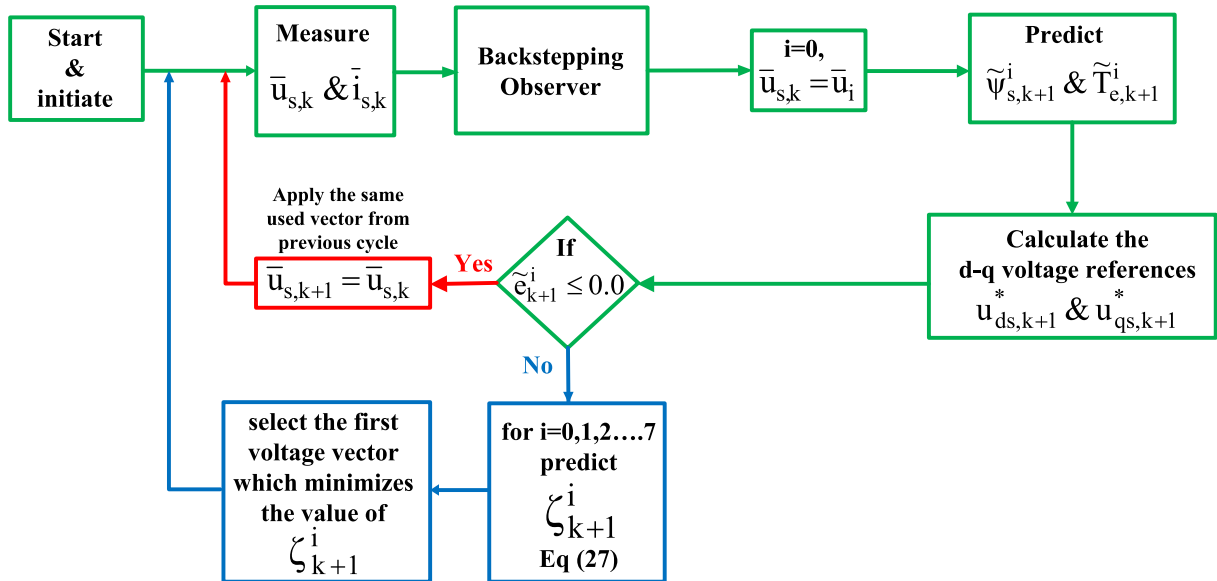
FIGURE 4. Implementation steps of the proposed sensorless PVC approach for IM drive.
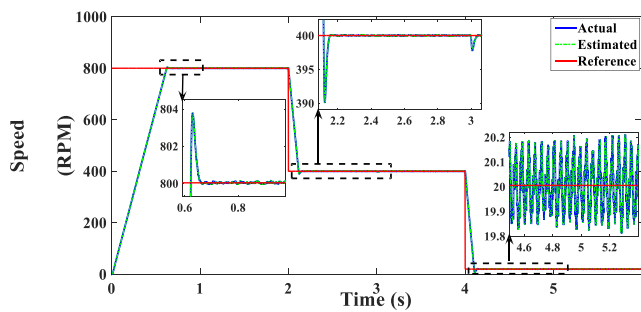
FIGURE 5. Speed profile for MP DTC (RPM).

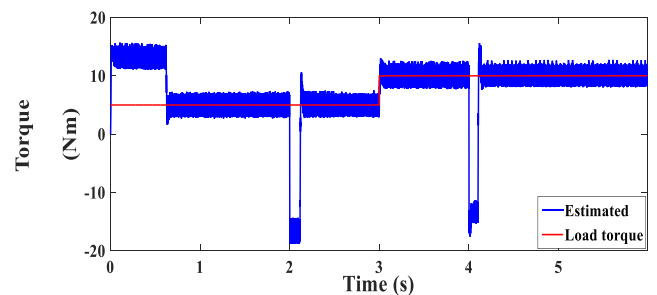**FIGURE 6.** Torque profile for MP DTC (Nm).
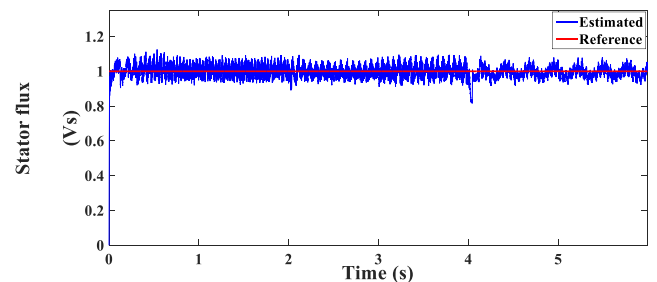
FIGURE 7. Stator flux profile for MP DTC (Vs).

The back-stepping technique is composed of two round; the first is concerned with designing a stable system for the integration of the estimation errors $(\tilde{h}_\alpha, \tilde{h}_\beta)$ utilizing $\tilde{i}_{\alpha s}$ and $\tilde{i}_{\beta s}$ as virtual control variables with their references of j_α and j_β which act as stabilizing functions. Then, the integration of the estimation errors $(\tilde{x}_\alpha, \tilde{x}_\beta)$ can be expressed by

$$\frac{d\tilde{x}_\alpha}{dt} = \tilde{i}_{\alpha s}, \quad \text{and} \quad \frac{d\tilde{x}_\beta}{dt} = \tilde{i}_{\beta s} \qquad (32)$$

Via utilizing (31) and (32), and by adding and subtracting j_α and j_β to/from these relationships, it results

$$\frac{d\tilde{x}_\alpha}{dt} = Z_\alpha - C_1\tilde{x}_\alpha, \quad \frac{d\tilde{x}_\beta}{dt} = Z_\beta - C_1\tilde{x}_\beta$$

where

$$Z_\alpha = \tilde{i}_{\alpha s} - j_\alpha, \quad Z_\beta = \tilde{i}_{\beta s} - j_\beta,$$

and

$$j_\alpha = -C_1\tilde{x}_\alpha, \quad j_\beta = -C_1\tilde{x}_\beta \qquad (33)$$

where C_1 is a positive value.

The second stage of back-stepping technique is concerned with controlling the variables Z_α and Z_β, which can be evaluated from (33) by

$$Z_\alpha = \tilde{i}_{\alpha s} + C_1\tilde{x}_\alpha, \text{ and } Z_\beta = \tilde{i}_{\beta s} + C_1\tilde{x}_\beta \qquad (34)$$

By differentiating (34), it results

$$\begin{aligned} \frac{dZ_\alpha}{dt} = {} & \frac{\tilde{R}_r L_m}{\sigma L_s L_r^2}\psi_{\alpha r} + \frac{\hat{R}_r L_m}{\sigma L_s L_r^2}\tilde{\psi}_{\alpha r} + \frac{L_m}{\sigma L_s L_r}\hat{\omega}_{me}\tilde{\psi}_{\beta r} \\ & + \frac{L_m}{\sigma L_s L_r}\tilde{\omega}_{me}\psi_{\beta r} - \frac{L_m^2\tilde{R}_r + L_r^2\tilde{R}_s}{\sigma L_s L_r^2}h_\alpha + s_\alpha + C_1\tilde{i}_{\alpha s} \end{aligned}$$

$$(35)$$
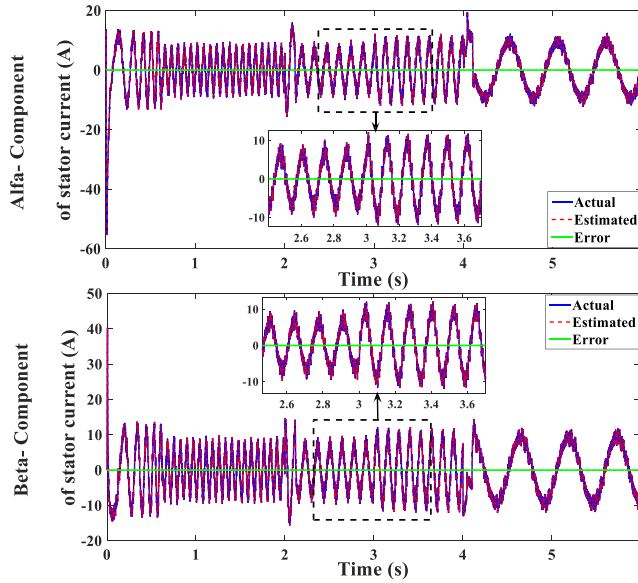
FIGURE 8. (a) α-component, (b) β-component of stator current for MP DTC (A).
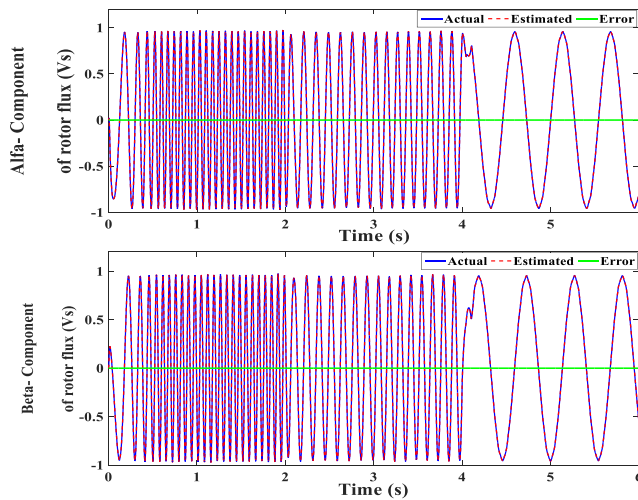
FIGURE 9. (a) α-component, (b) β-component of rotor flux for MP DTC (Vs).
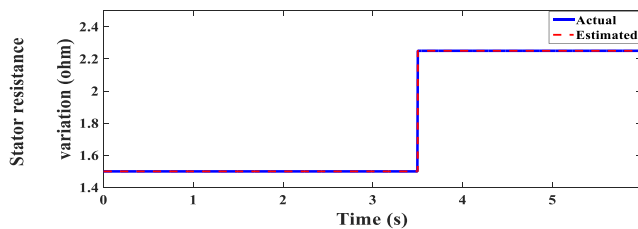
FIGURE 10. Stator resistance variation (Ω).

$$\frac{dZ_\beta}{dt} = \frac{\tilde{R}_r L_m}{\sigma L_s L_r^2}\psi_{\beta r} + \frac{\hat{R}_r L_m}{\sigma L_s L_r^2}\tilde{\psi}_{\beta r} - \frac{L_m}{\sigma L_s L_r}\hat{\omega}_{me}\tilde{\psi}_{\alpha r}$$
$$-\frac{L_m}{\sigma L_s L_r}\tilde{\omega}_{me}\psi_{\alpha r} - \frac{L_m^2\tilde{R}_r + L_r^2\tilde{R}_s}{\sigma L_s L_r^2}h_\beta + s_\beta + C_1\tilde{i}_{\beta s}$$

(36)
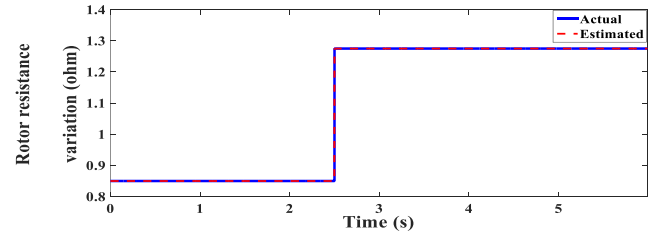
FIGURE 11. Rotor resistance variation (Ω).
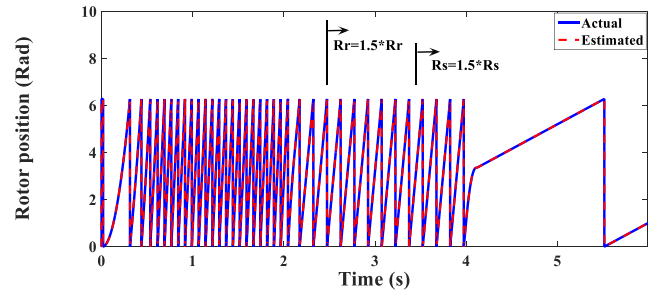
FIGURE 12. Rotor position for MP DTC (Rad).
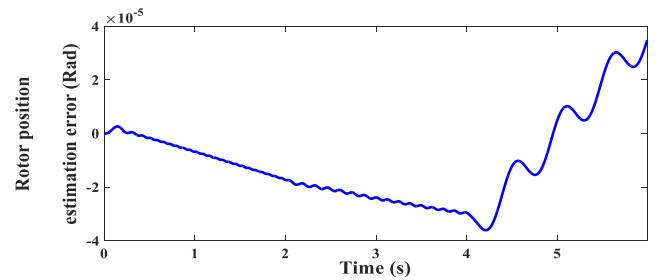
FIGURE 13. Position's estimation error under MP DTC (Rad).
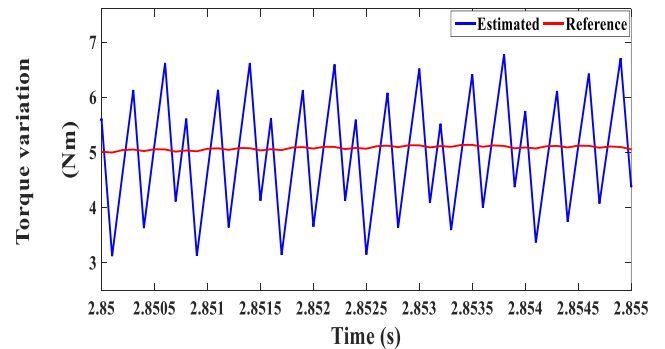
FIGURE 14. Detailed view of torque variation for MP DTC (Nm).

The control inputs s_α and s_β can be evaluated as follows

$$s_\alpha = -\frac{\hat{R}_r L_m}{\sigma L_s L_r^2}\tilde{\psi}_{\alpha r} - \frac{L_m}{\sigma L_s L_r}\hat{\omega}_{me}\tilde{\psi}_{\beta r} - C_1\tilde{i}_{\alpha s} - C_2 Z_\alpha - \tilde{x}_\alpha$$

$$s_\beta = -\frac{\hat{R}_r L_m}{\sigma L_s L_r^2}\tilde{\psi}_{\beta r} + \frac{L_m}{\sigma L_s L_r}\hat{\omega}_{me}\tilde{\psi}_{\alpha r} - C_1\tilde{i}_{\beta s} - C_2 Z_\beta - \tilde{x}_\beta$$

(37)

where C_2 is a positive constant.
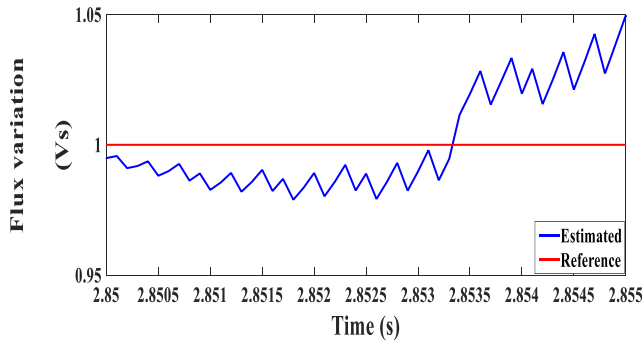
FIGURE 15. Detailed view of stator flux variation for MP DTC (Vs).
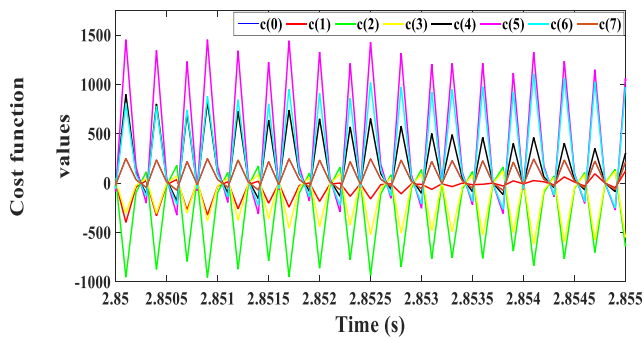
FIGURE 16. Detailed view of cost function's values for MP DTC.
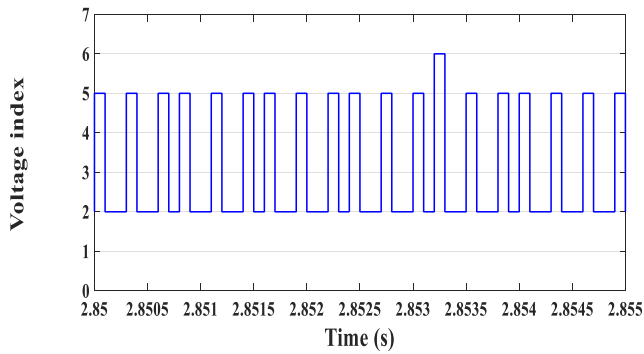
FIGURE 17. Detailed view of selected voltage index for MP DTC.
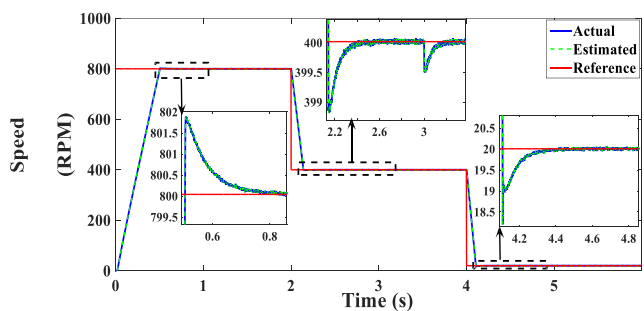
FIGURE 18. Rotor speed under PVC (RPM).

FIGURE 19. Developed torque under PVC (Nm).
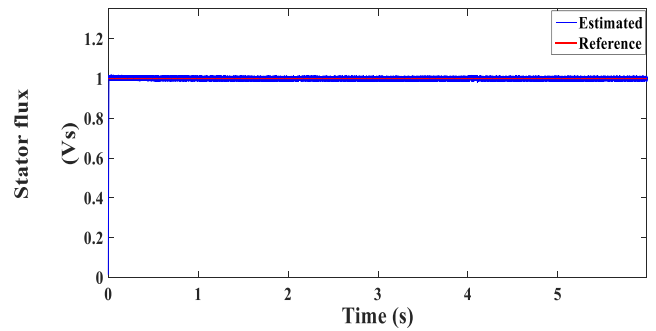
FIGURE 20. Stator flux under PVC (Vs).
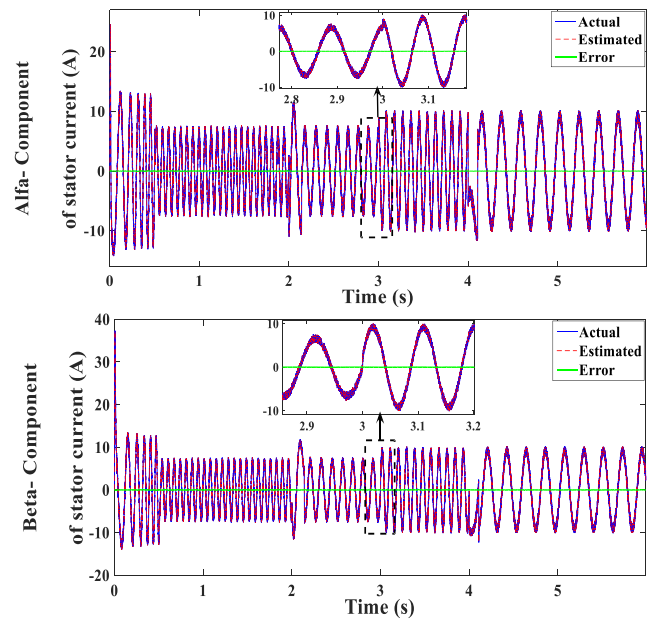
FIGURE 21. (a) α-component, (b) β-component of stator current under PVC (A).

Then, by substituting from (37) into (35) and (36), it results

$$\frac{dZ_\alpha}{dt} = \frac{\tilde{R}_r L_m}{\sigma L_s L_r^2}\psi_{\alpha r} + \frac{L_m}{\sigma L_s L_r}\tilde{\omega}_{me}\psi_{\beta r}$$

$$-\frac{L_m^2 \tilde{R}_r + L_r^2 \tilde{R}_s}{\sigma L_s L_r^2}h_\alpha - C_2 Z_\alpha - \tilde{x}_\alpha$$

$$\frac{dZ_\beta}{dt} = \frac{\tilde{R}_r L_m}{\sigma L_s L_r^2}\psi_{\beta r} - \frac{L_m}{\sigma L_s L_r}\tilde{\omega}_{me}\psi_{\alpha r}$$

$$-\frac{L_m^2 \tilde{R}_r + L_r^2 \tilde{R}_s}{\sigma L_s L_r^2}h_\beta - C_2 Z_\beta - \tilde{x}_\beta \quad (38)$$
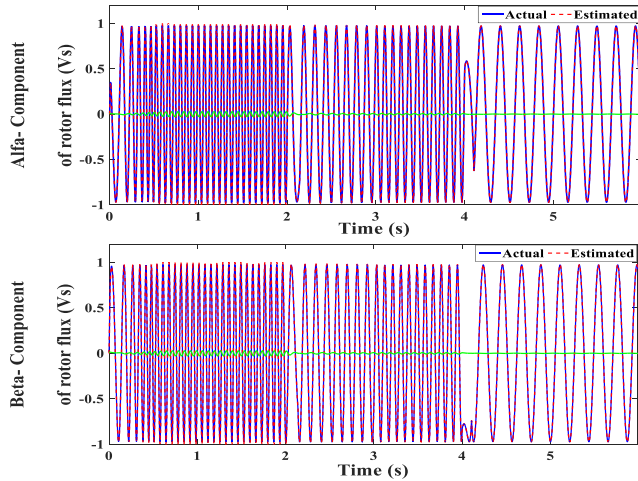
FIGURE 22. (a) α-component, (b) β-component of rotor flux under PVC (Vs).
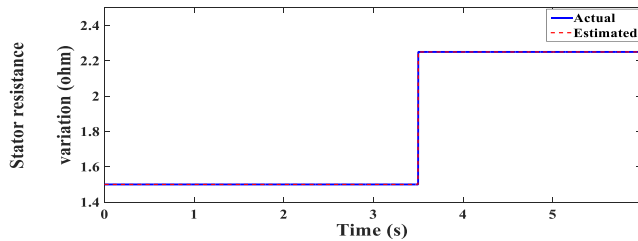
FIGURE 23. Stator resistance variation under PVC (Ω).
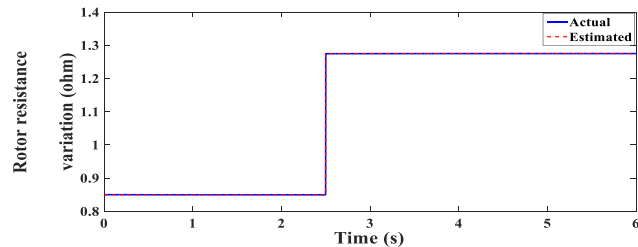
FIGURE 24. Rotor resistance variation under PVC (Ω).
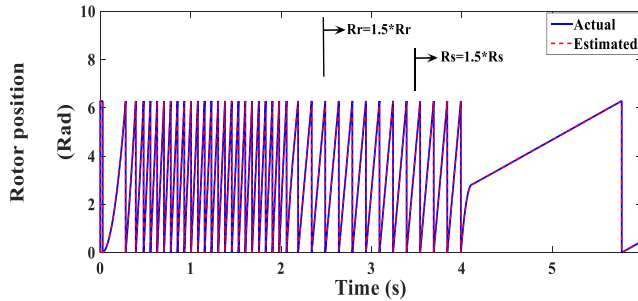
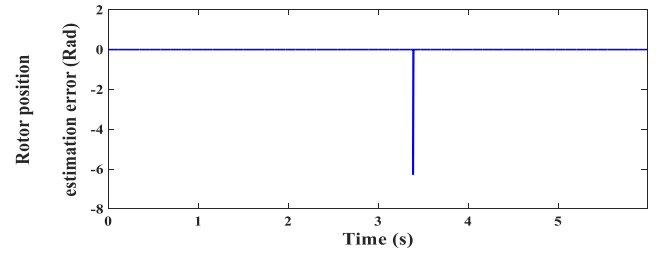**FIGURE 25.** Rotor position under PVC (Rad).
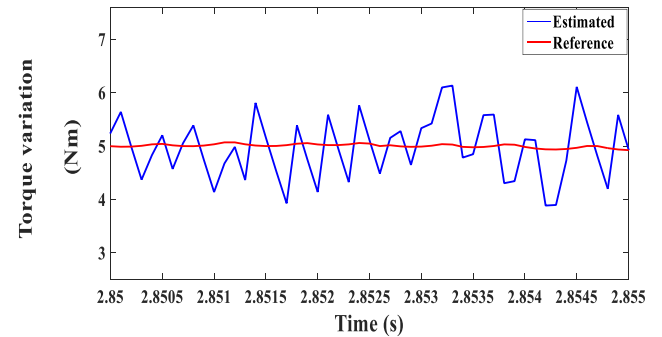

FIGURE 26. Position's estimation error under PVC (Rad).

FIGURE 27. Detailed torque variation under PVC (Nm).
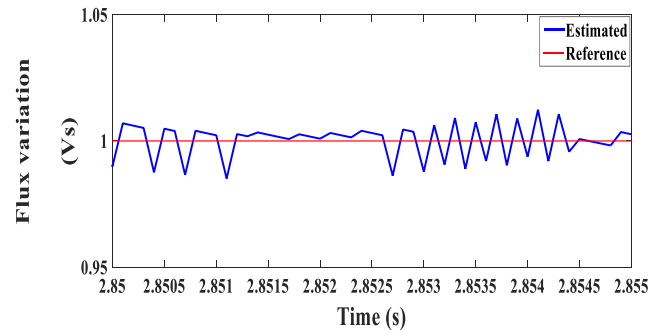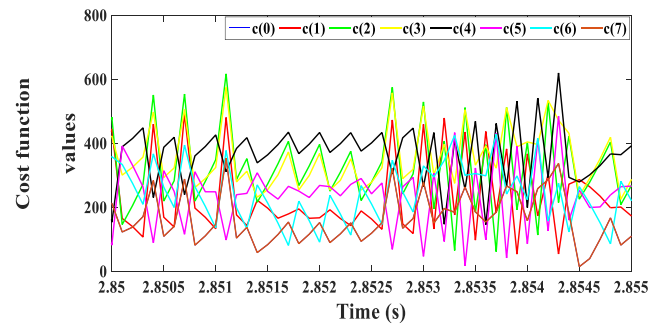

FIGURE 28. Detailed flux variation under PVC (Vs).

FIGURE 29. Detailed view of cost function's values under PVC.

The observer's stability analysis is performed using the Lyapunov preference defined by

$$V = \frac{1}{2}\left\{ \tilde{x}_\alpha^2 + \tilde{x}_\beta^2 + \tilde{Z}_\alpha^2 + \tilde{Z}_\beta^2 + \tilde{\psi}_{\alpha r}^2 \right.$$
$$\left. + \tilde{\psi}_{\beta r}^2 + \frac{1}{\Gamma_\omega}\tilde{\omega}_{me}^2 + \frac{1}{\Gamma_s}\tilde{R}_s^2 + \frac{1}{\Gamma_r}\tilde{R}_r^2 \right\} \quad (39)$$

where Γ_ω, Γ_s, Γ_r are positive quantities.

By differentiating (39), and substituting from (31), (33), (35) and (36), it results

$$\frac{dV}{dt} = -C_1\tilde{x}_\alpha^2 - C_1\tilde{x}_\beta^2 - C_2\tilde{Z}_\alpha^2 - C_2\tilde{Z}_\beta^2 - \frac{\hat{R}_r}{L_r}\tilde{\psi}_{\alpha r}^2 - \frac{\hat{R}_r}{L_r}\tilde{\psi}_{\beta r}^2$$
$$+ \tilde{R}_s\left\{ -\frac{L_r^2}{\sigma L_s L_r^2}Z_\alpha h_\alpha - \frac{L_r^2}{\sigma L_s L_r^2}Z_\beta h_\beta + \frac{1}{\Gamma_s}\frac{d\tilde{R}_s}{dt} \right\}$$

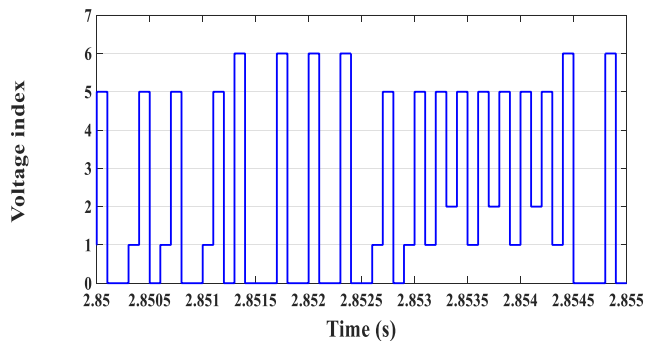**FIGURE 30.** Detailed view of selected voltage index under PVC.

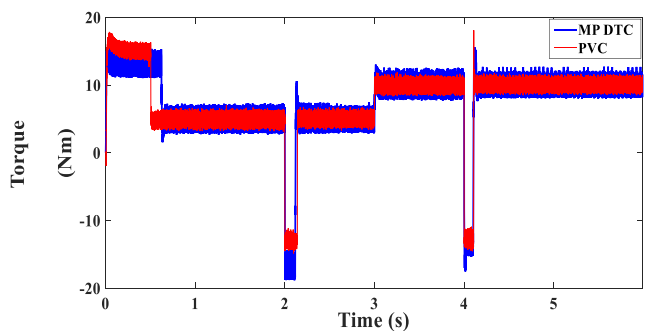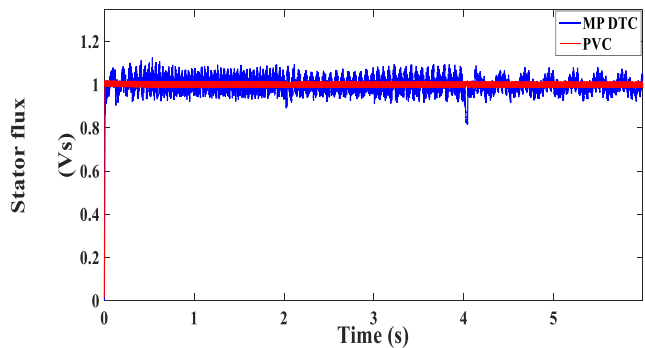**FIGURE 31.** Torque dynamics for the two approaches (Nm).

FIGURE 32. Flux dynamics for the two approaches (Vs).

FIGURE 33. Flux loci for the two controllers.
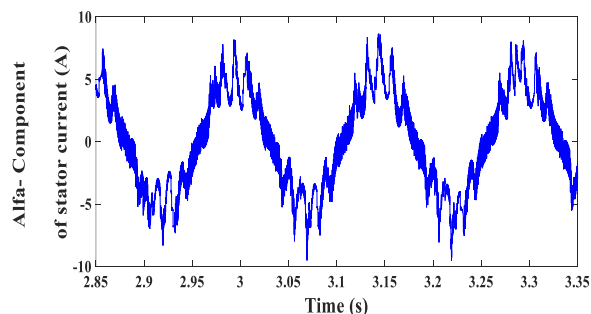
FIGURE 34. α-component current for MP DTC (A).
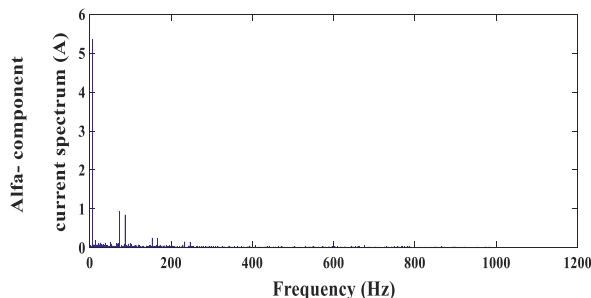
FIGURE 35. α-component current spectrum for MP DTC.

$$+ \tilde{R}_r \left\{ \frac{L_m}{\sigma L_s L_r^2} Z_\alpha \psi_{\alpha r} - \frac{L_m^2}{\sigma L_s L_r^2} Z_\alpha h_\alpha + \frac{L_m}{\sigma L_s L_r^2} Z_\alpha \psi_{\beta r} \right.$$

$$- \frac{L_m^2}{\sigma L_s L_r^2} Z_\beta h_\beta - \frac{\tilde{\psi}_{\alpha r} \psi_{\alpha r}}{L_r} + \frac{L_m}{L_r} h_\alpha \tilde{\psi}_{\alpha r} - \frac{\tilde{\psi}_{\beta r} \psi_{\beta r}}{L_r}$$

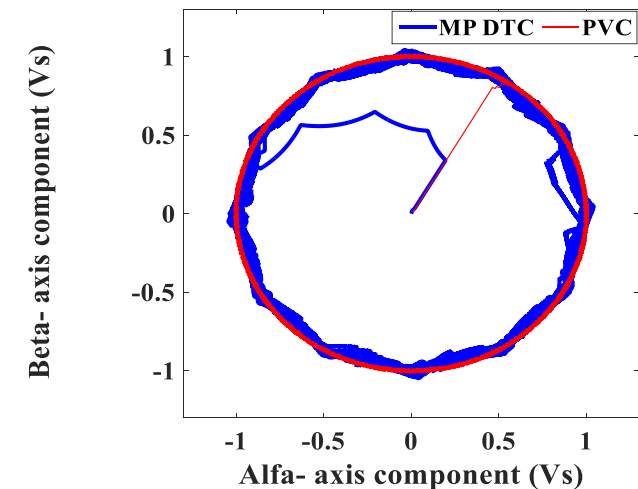$$\left. + \frac{L_m}{L_r} h_\beta \tilde{\psi}_{\beta r} + \frac{1}{\Gamma_r} \frac{d\tilde{R}_r}{dt} \right\}$$

$$+ \tilde{\omega}_{me} \left\{ \frac{L_m}{\sigma L_s L_r} \psi_{\beta r} - \frac{L_m}{\sigma L_s L_r} \psi_{\alpha r} + \frac{1}{\Gamma_\omega} \frac{d\tilde{\omega}_{me}}{dt} \right\} \quad (40)$$

The Lyapunov preference V is positive definite, and thus to get a negative variation of V, the next states must be fulfilled

$$\tilde{R}_s \left\{ -\frac{L_r^2}{\sigma L_s L_r^2} Z_\alpha h_\alpha - \frac{L_r^2}{\sigma L_s L_r^2} Z_\beta h_\beta + \frac{1}{\Gamma_s} \frac{d\tilde{R}_s}{dt} \right\} = 0.0 \quad (41)$$

$$\tilde{R}_r \left\{ \frac{L_m}{\sigma L_s L_r^2} Z_\alpha \psi_{\alpha r} - \frac{L_m^2}{\sigma L_s L_r^2} Z_\alpha h_\alpha + \frac{L_m}{\sigma L_s L_r^2} Z_\alpha \psi_{\beta r} \right.$$

$$- \frac{L_m^2}{\sigma L_s L_r^2} Z_\beta h_\beta - \frac{\tilde{\psi}_{\alpha r} \psi_{\alpha r}}{L_r} + \frac{L_m}{L_r} h_\alpha \tilde{\psi}_{\alpha r}$$

$$\left. - \frac{\tilde{\psi}_{\beta r} \psi_{\beta r}}{L_r} + \frac{L_m}{L_r} h_\beta \tilde{\psi}_{\beta r} + \frac{1}{\Gamma_r} \frac{d\tilde{R}_r}{dt} \right\} = 0.0 \quad (42)$$

$$\tilde{\omega}_{me} \left\{ \frac{L_m}{\sigma L_s L_r} \hat{\psi}_{\beta r} - \frac{L_m}{\sigma L_s L_r} \hat{\psi}_{\alpha r} + \frac{1}{\Gamma_\omega} \frac{d\tilde{\omega}_{me}}{dt} \right\} = 0.0 \quad (43)$$

This results in expressing the adaptation laws for the stator resistance, rotor resistance and speed as following

$$\frac{d\tilde{R}_s}{dt} = \Gamma_s \left\{ \frac{L_r^2}{\sigma L_s L_r^2} Z_\alpha h_\alpha + \frac{L_r^2}{\sigma L_s L_r^2} Z_\beta h_\beta \right\} \quad (44)$$
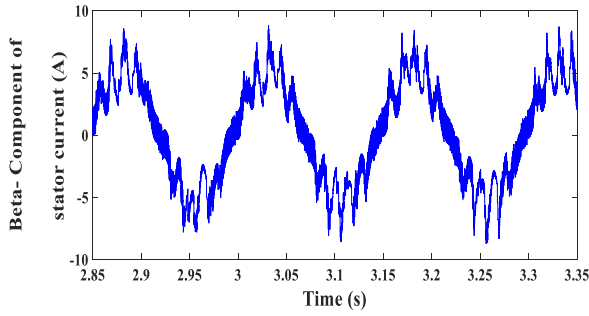
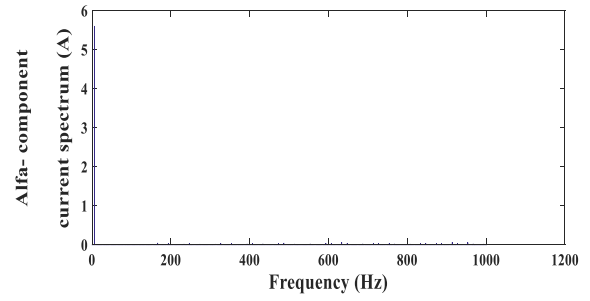**FIGURE 36.** β-component current for MP DTC (A).

FIGURE 37. β-component spectrum for MP DTC.

FIGURE 38. α-component current for PVC (A).

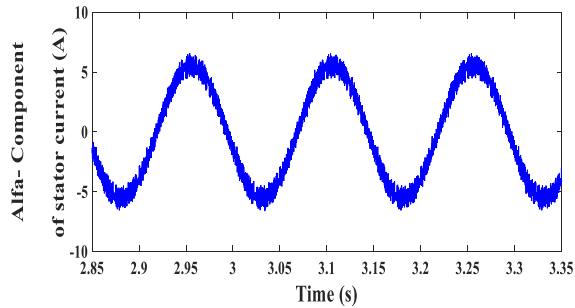**FIGURE 39.** α-component current spectrum for PVC.
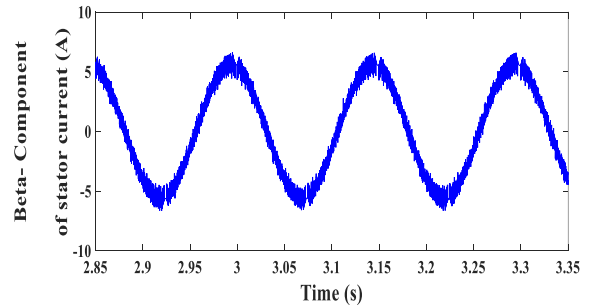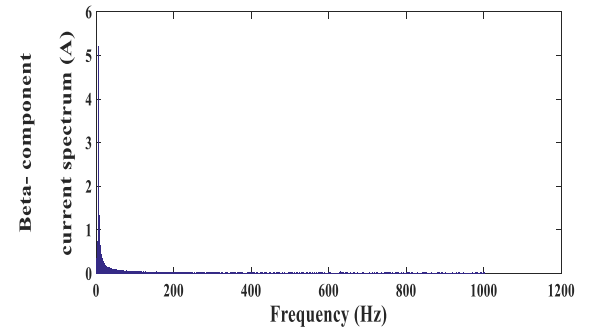

FIGURE 40. β-component current for PVC (A).

FIGURE 41. β-component spectrum for PVC.

$$\frac{d\tilde{R}_r}{dt} = \Gamma_r \left\{ \frac{-L_m}{\sigma L_s L_r^2} Z_\alpha \psi_{\alpha r} + \frac{L_m^2}{\sigma L_s L_r^2} Z_\alpha h_\alpha - \frac{L_m}{\sigma L_s L_r^2} Z_\alpha \psi_{\beta r} \right.$$
$$+ \frac{L_m^2}{\sigma L_s L_r^2} Z_\beta h_\beta + \frac{\tilde{\psi}_{\alpha r} \psi_{\alpha r}}{L_r} - \frac{L_m}{L_r} h_\alpha \tilde{\psi}_{\alpha r}$$
$$\left. + \frac{\tilde{\psi}_{\beta r} \psi_{\beta r}}{L_r} - \frac{L_m}{L_r} h_\beta \tilde{\psi}_{\beta r} \right\} \tag{45}$$

$$\frac{d\tilde{\omega}_{me}}{dt} = \Gamma_\omega \left\{ \frac{L_m}{\sigma L_s L_r} \hat{\psi}_{\alpha r} - \frac{L_m}{\sigma L_s L_r} \hat{\psi}_{\beta r} \right\} \tag{46}$$

Then by using (44), (45) and (46), the speed and resistances can be accurately estimated. A general layout for the back-stepping observer illustrating the inputs and outputs is illustrated in Figure 2.

V. COMPLETE SYSTEM LAYOUT
After designing the BSO observer, the complete control system is constructed and formulated as shown in Figure 3.

The system measures and samples the currents of the stator windings to be used by the controller besides the feedback voltages which are obtained with the help of FCS mechanism. The input to the proposed BSO observer are the sampled voltages and currents, while the outputs are the estimated signals of the current, flux, speed and stator and rotor resistances. After that, the observed speed is used to close the speed loop, while the observed stator current and rotor flux are used to evaluate the stator flux using the current-flux relationship. The estimated signals including the resistances are then used to predict the torque and flux at $(k+1)_{T_s}$, which are then substracted from their references to get the error signals which are the inputs to the PI flux and torque regulators.

The PI regulators are then used to provide the reference voltages $u^*_{ds,k+1}$ and $u^*_{qs,k+1}$ which are then used by the convergence condition of (27). The feedback voltage signals $u_{ds,k+1}$ and $u_{qs,k+1}$ are obtained from the controller outputs using a memory block which is considered as a buffering unit.
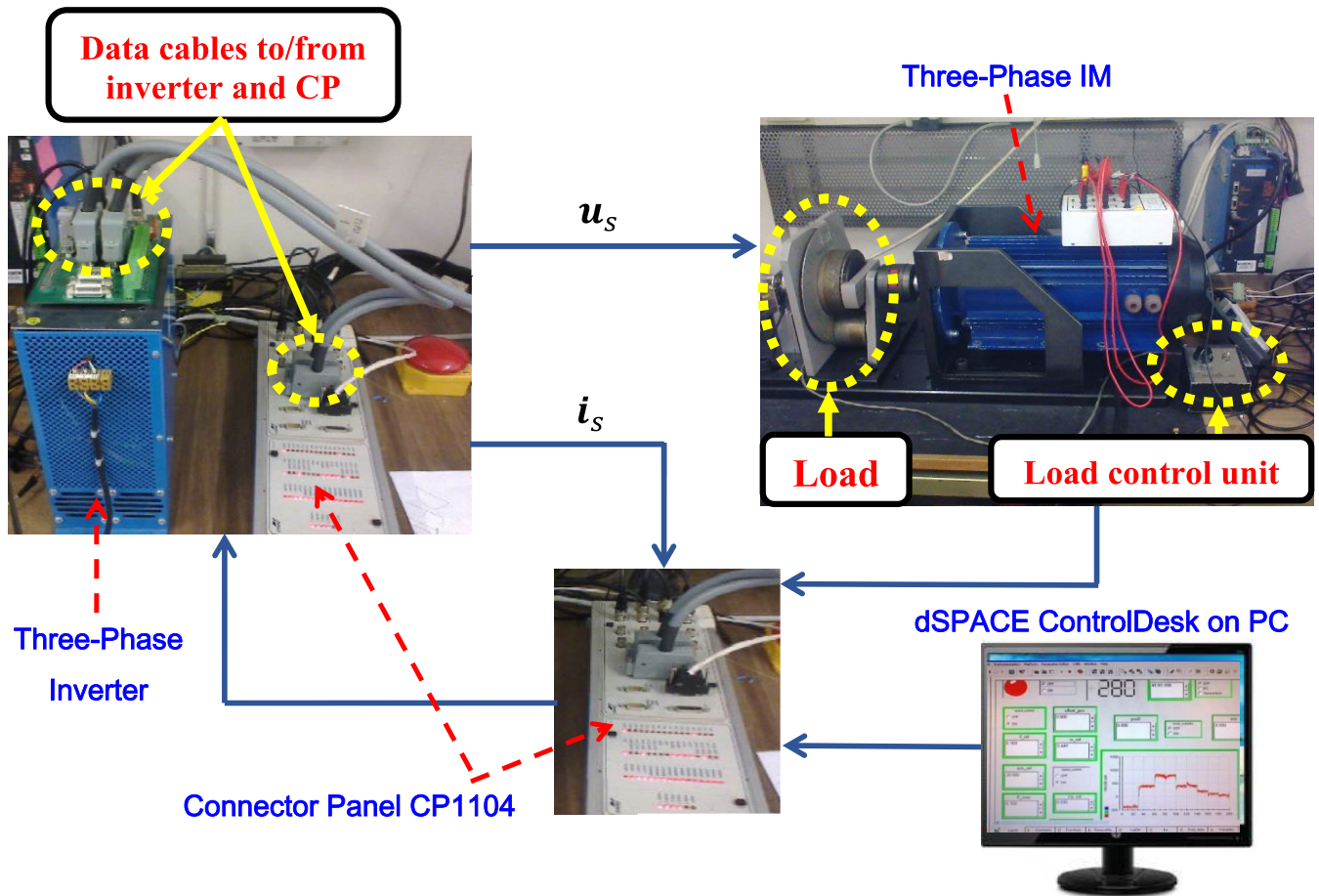
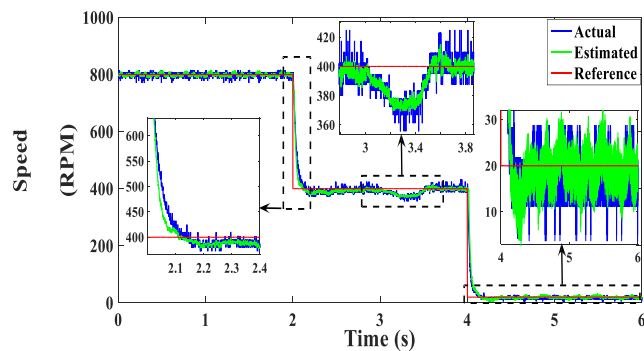**FIGURE 42.** Experimental layout for the proposed PVC approach.

FIGURE 43. Rotor speed with MP DTC (RPM).

FIGURE 44. Developed torque with MP DTC (Nm).

The implementation steps of the designed PVC procedure is presented in Fig. 4, in which the control systems starts with setting initial values, then the measurement and sampling of the voltages and currents are performed, after that the BSO is utilized to estimate the required variables which are then used to predict the torque and stator flux at time $(k+1)T_s$. The predicted variables are then used along with the torque and flux references to get the reference voltages using the designed regulators. The next step is the substitution of the reference and predicted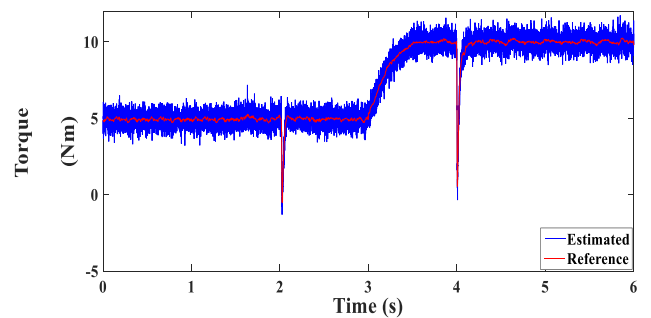 signals into the designed cost function and starting the optimization until a minimum value is obtained, then the specified voltage which achieves this target is chosen by the controller.

VI. SIMULATION RESULTS

In order to test the applicability of the PVC, a comparative study is organized between the performances of the MP DTC and novel PVC approaches. The Matlab/Simulink software is firstly used for comparing the two dynamic performances and then the experimental tests are carried out using a dSPACE
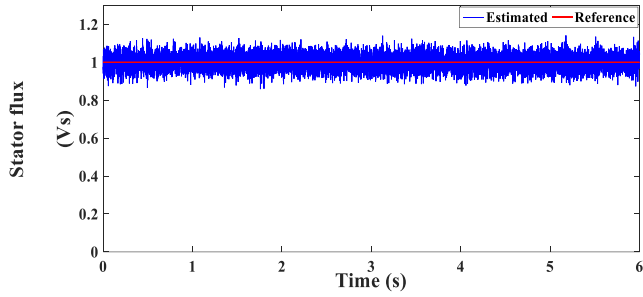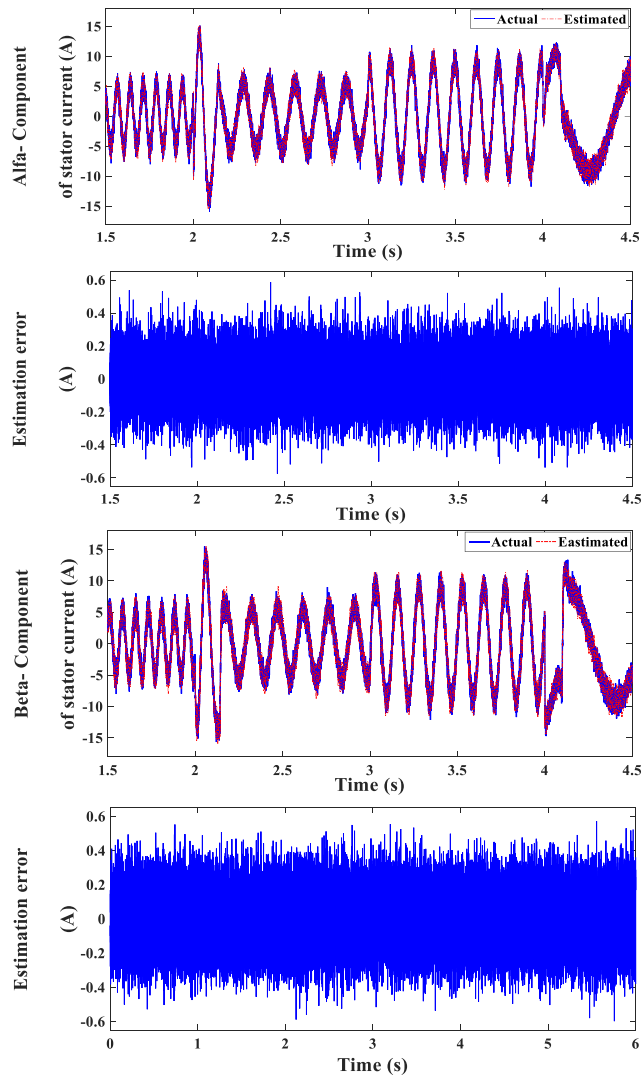
FIGURE 45. Stator flux with MP DTC (Vs).

FIGURE 46. Actual and estimated α- β-components of stator current and the resulatant errors with MP DTC (A).

FIGURE 47. Actual and estimated α- β-components of rotor flux and the resulatant errors with MP DTC (A).
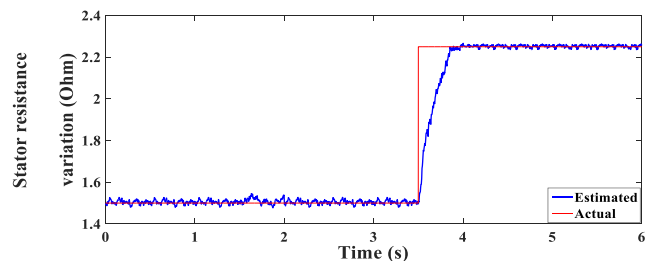
FIGURE 48. Stator resistance change with MP DTC (Ω).

1104 control board as presented in Sect. 7. The tests are concerned with checking the dynamic response and testing the validity of the sensorless scheme. The tests are arranged for a speed variation of $800 \rightarrow 400 \rightarrow 20$ RPM at t = 0s, t = 2 s and t = 4 s, respectively. A load torque of 5 Nm (half of rated torque) is applied at starting, then it is changed to
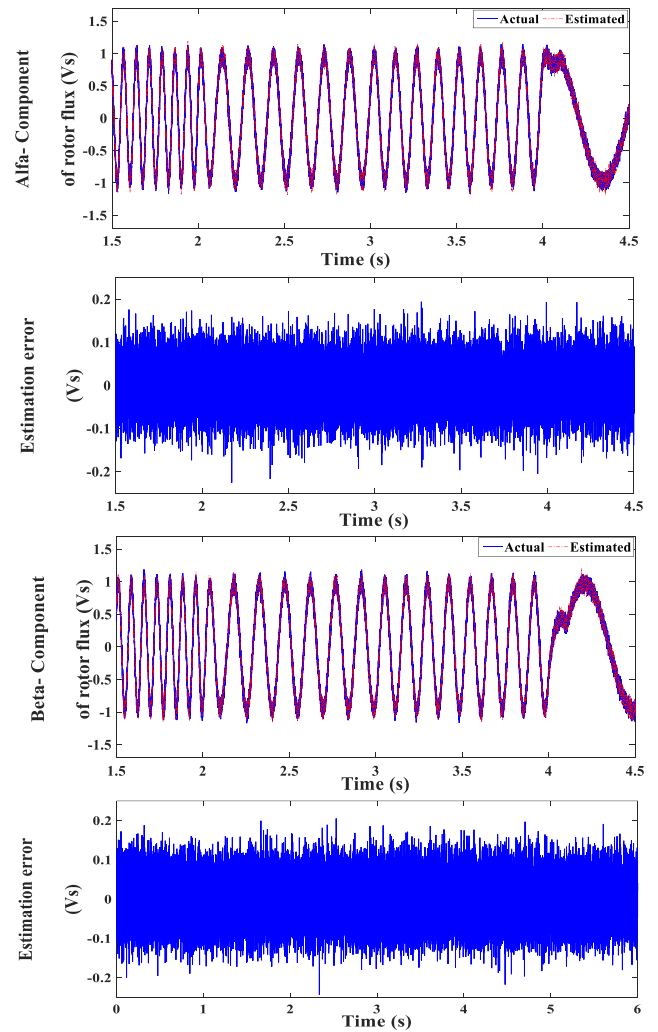
full load (10 Nm) at t = 3.5 s. The reference flux is set to the rated flux (1 Vs). In order to test the BSO robustness against parameters variation, a change in the stator resistance (R_s) is made at time t = 3.5 s at which R_s became 1.5 times of its original value. In similar way, the rotor resistance (R_r) value is changed at time t = 2.5 s to be 1.5 times of its original value. The BSO performance is tested for different speed ranges for the two control approaches.
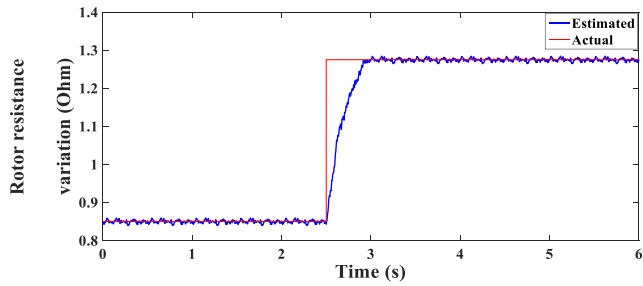
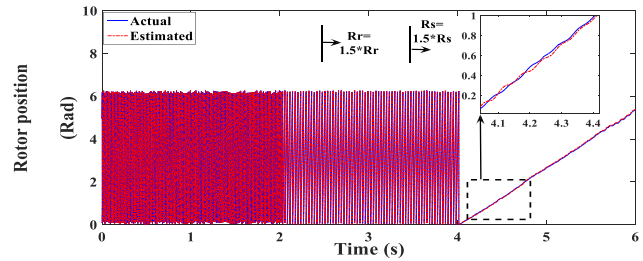**FIGURE 49.** Rotor resistance change with MP DTC (Ω).

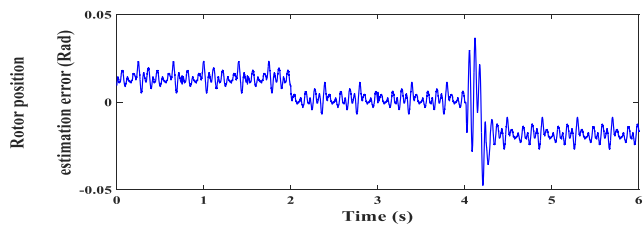**FIGURE 50.** Rotor position with MP DTC (Rad).

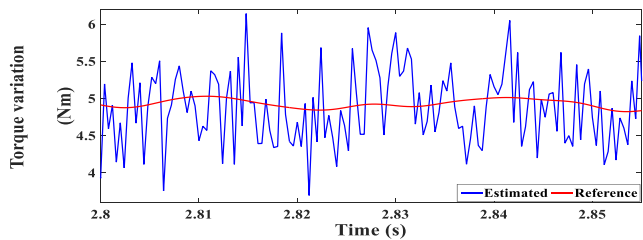**FIGURE 51.** Position's estimation error with MP DTC (Rad).

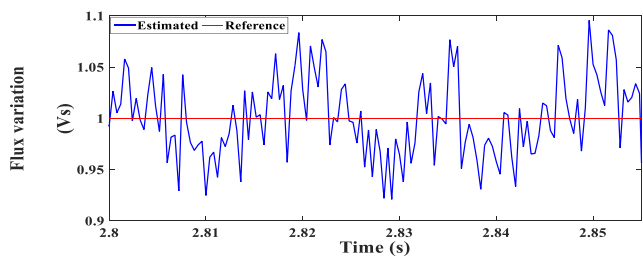**FIGURE 52.** Detailed torque variation with MP DTC (Nm).

FIGURE 53. Detailed flux variation with MP DTC (Vs).

A. PERFORMANCE OF MP DTC WITH BSO

At first, the dynamics of IM using the MP DTC are presented as shown in Figures 5, 6 and 7 which illustrate the speed, the developed torque and stator flux profiles, in turn. In Figure 5, the validness of the proposed BSO for the precise
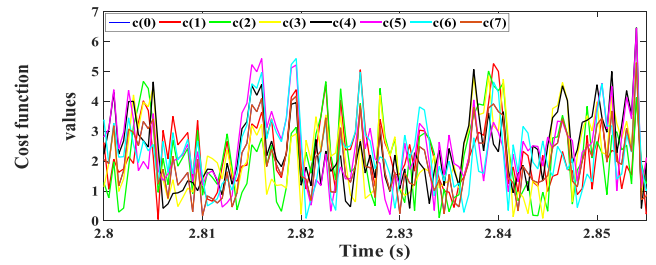
FIGURE 54. Detailed view of cost function's values with MP DTC.
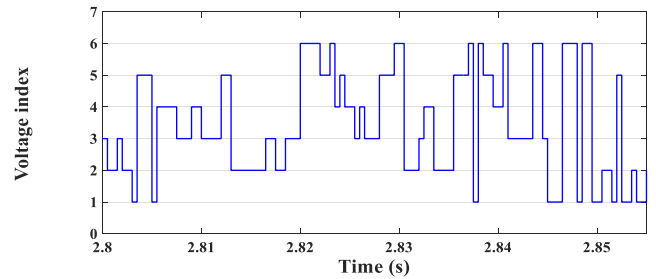
FIGURE 55. Detailed view of selected voltage index with MP DTC.
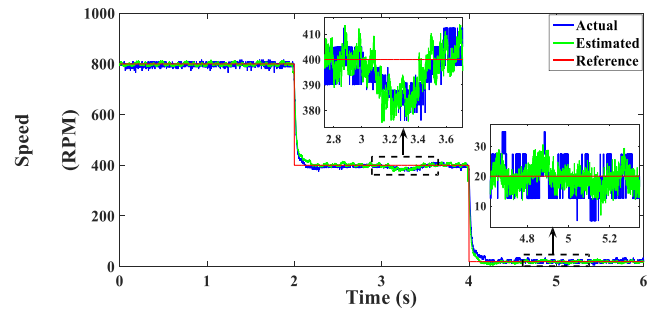
FIGURE 56. Rotor speed with PVC (RPM).
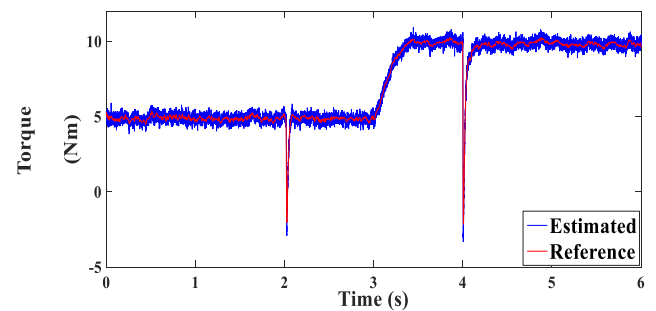
FIGURE 57. Developed torque with PVC (Nm).

speed estimation is confirmed at very low speed operation and under parameters mismatch as well. However, the ripples are noticeable under the MP DTC.

The BSO is still confirming its effectiveness with the MP DTC, and this is illustrated through Figs. 8 (a,b) and 9 (a,b) which show the actual and evaluated signals of the current and flux, accordingly. Figures 10 and 11 show the estimated and actual values of stator and rotor resistances which reconfirm the validity of the BSO.
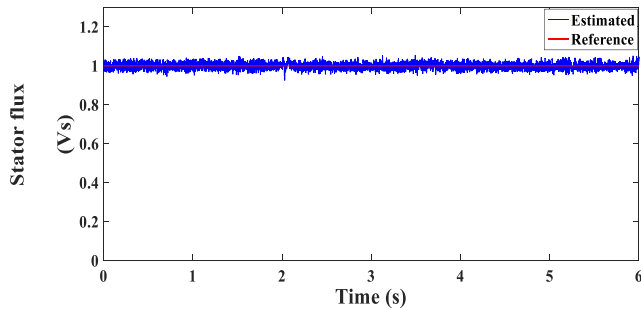
FIGURE 58. Stator flux with PVC (Vs).

The robustness of the BSO is verified through the correct estimation of rotor position θ_{me} while changing the parameters. This is observed in Figure 12 which presents the actual and calculated positions and Figure 13 which presents the resultant error. From these illustrations, it can be realized that there is a definite alignment between the actual and estimated positions which resulted in a null estimation error.

In order to perform the comparison in an appropriate way, the control action under the two approaches must be illustrated in detailed figures. So, for the MP DTC, the control action is illustrated through Figures 14, 15, 16 and 17 which show a detailed view of torque variation, flux variation, cost function (28) and voltage index.

B. PERFORMANCE OF PROPOSED PVC WITH BSO

The drive performance is also analyzed using the sensorless PVC approach. The tests are performed with the same terms introduced in Sect. VI (A) where the MP DTC was adopted. The IM dynamics under PVC are shown in Figures 18, 19 and 20 which show the speed, torque and flux profiles. The BSO is confirming its validity with the PVC approach via the accurate estimation of the speed at different speed operation and under system's uncertainties as well. Meanwhile, in Figures, 19 and 20, it can be obviously noticed that the ripples are effectively suppressed in comparison with its relative values under the MP DTC approach in Figures 6 and 7.

The reduced ripples content is also noticed in the estimated and actual signals of the currents and fluxes as seen in Figures. 21 (a,b) and 22 (a,b). Through these figures, the robustness of the BSO is also proved through the precise estimation of current and flux components.

Figures 23 and 24 illustrate the observed and actual values of the resistances. Using the BSO, the variations in the resistances are effectively observed and tracked with minimum deviation.

The BSO robustness is also tested with the PVC approach through the accurate observation of rotor position under the parameters mismatch as shown in Figures 25 and 26.

A zoomed layout for the torque and flux dynamics are shown in Figures 27, 28, 29 and 30 that show the detailed torque variation, detailed flux variation, calculated cost functions and voltage index. From these figures and by comparing
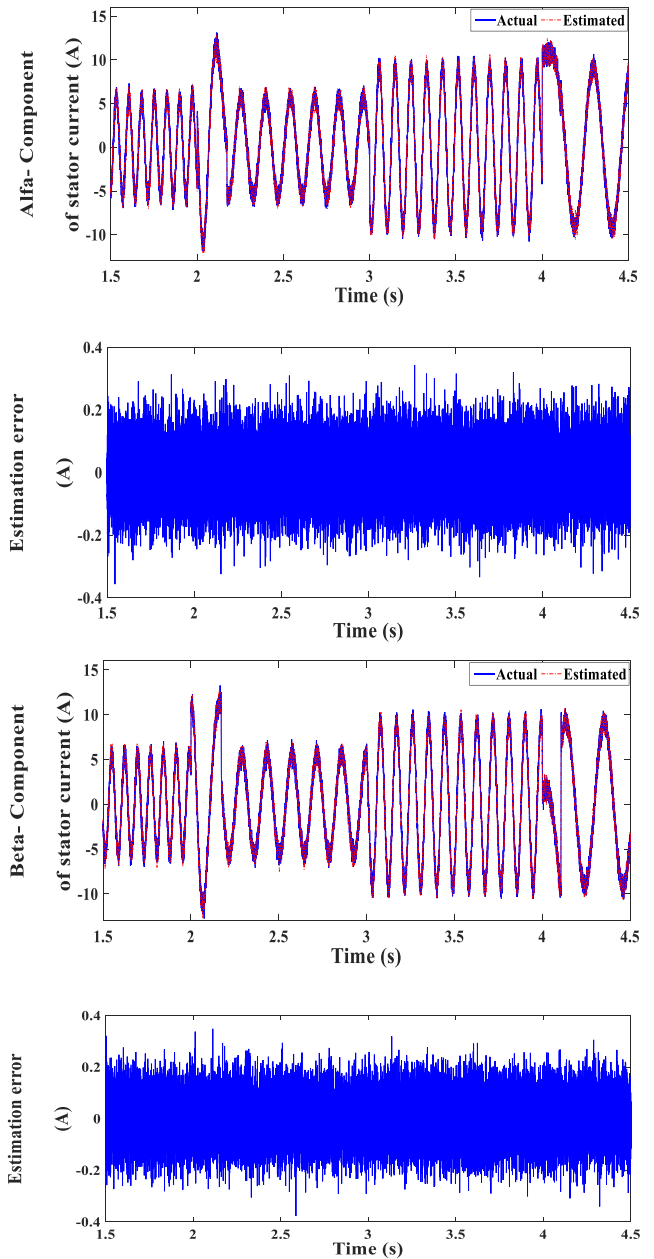
FIGURE 59. Real and observed α- β-components of stator current and the resulatant errors with PVC (A).

with their relatives quantities under MP DTC, it can be realized that the ripples under the PVC are effectively reduced.

The performances of the two control procedure can be also shown in the same figure to visualize the advantage of the PVC over the MP DTC in the context of reduced torque and flux ripples. Figures 31, 32 and 33 show the torque, flux and iso flux profiles for the two approaches. It can be also noted that the dynamic response for the proposed PVC is faster than the MP DTC and this due to that the control terms of the cost function used by the PVC are the stator voltages which are not calculated values like the flux and torque in the MP DTC, so the time to reach to the target is much shorter when using PVC.

FIGURE 60. Real and observed α- β-components of rotor flux and the resultant errors with PVC (Vs).

FIGURE 61. Stator resistance change with PVC (Ω).

FIGURE 62. Rotor resistance change with PVC (Ω).
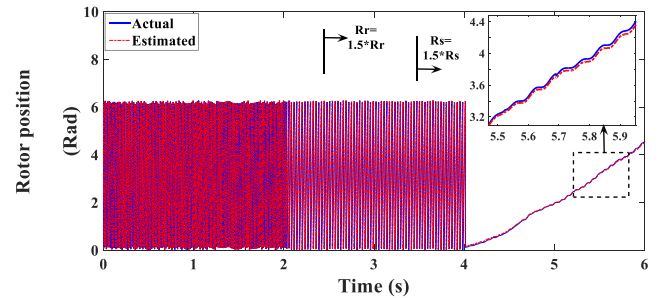
FIGURE 63. Rotor position with PVC (Rad).
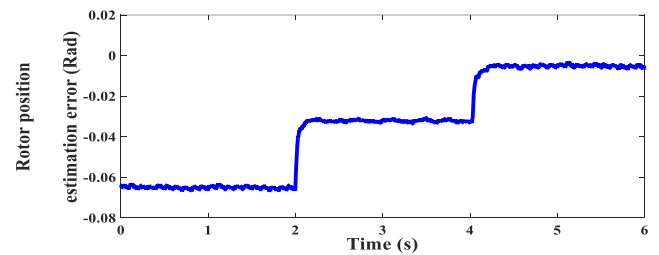
FIGURE 64. Position's estimation error with PVC (Rad).
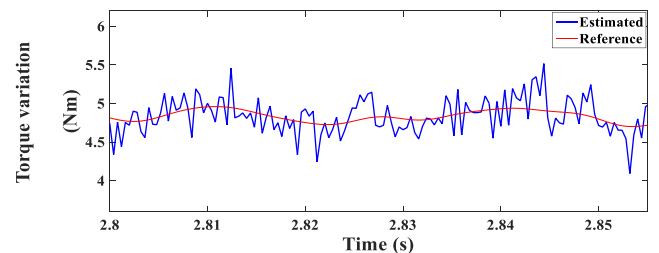
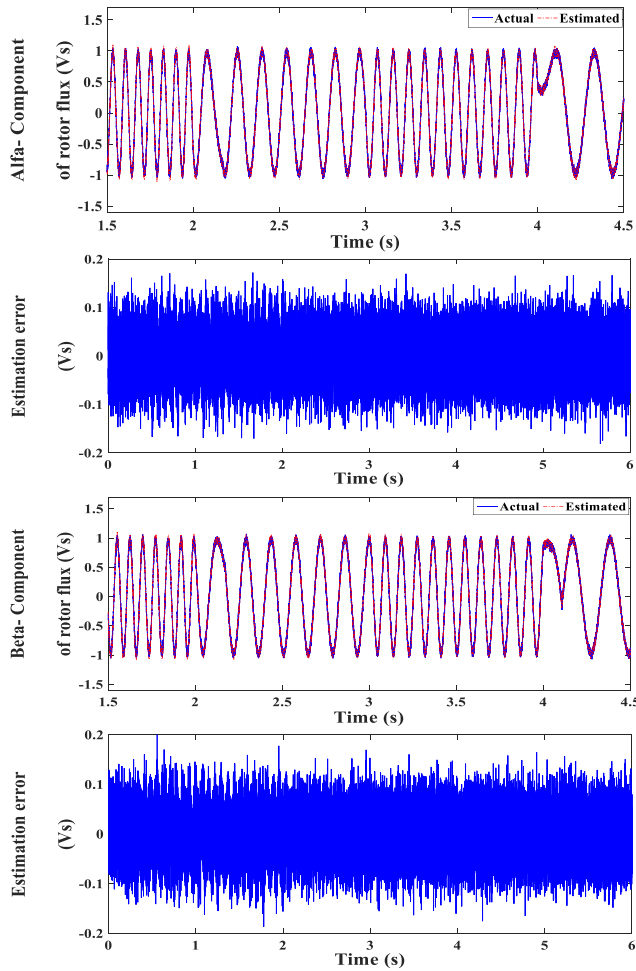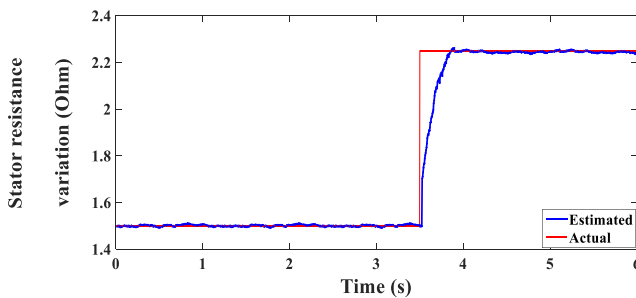**FIGURE 65.** Detailed torque variation with PVC (Nm).

TABLE 1. Currents spectrums under MP DTC and PVC approaches (simulation).

Algorithm	current spectrums	
	$i_{\alpha s}$	$i_{\beta s}$
MP DTC	Fundamental (5.34837A) THD= 3.45 %	Fundamental (5.30617 A) THD= 3.74 %
PVC	Fundamental (5.6032 A) THD= 0.50 %	Fundamental (5.60095 A) THD= 0.52 %

The comparison is also performed through analyzing the harmonics content in the stator voltage and stator current signals using the Fast Fourier Transform (FFT) analysis. Figures 34, 35, 36 and 37 show the α-components of stator current and stator voltage and their respective FFT spectrums when applying the MP DTC approach. Meanwhile, Figures 38, 39, 40 and 41 illustrate the current signals and the related FFT analysis when applying the proposed PVC approach. By visual check it is not difficult to distinguish the reduced current and voltage harmonics when
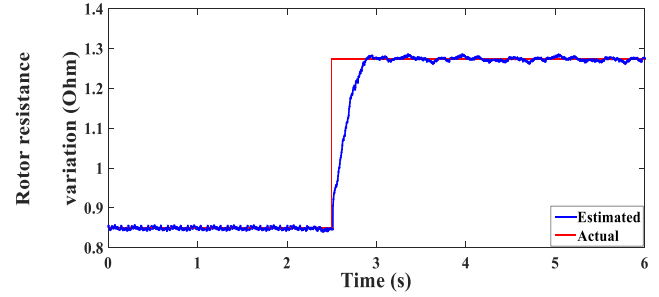
applying the PVC in contrast to the values obtained under MP DTC.

The Table 1 shows the FFT analysis for the current signals which are obtained by the two control approaches.

TABLE 2. Number of commutations for both techniques.

Technique	Commutations	Switching frequency
MP DTC	11090	1.850 KHz
PVC	5423	904 Hz
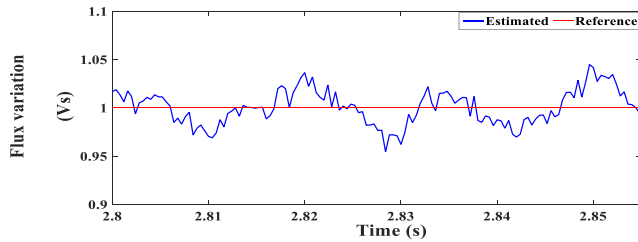
FIGURE 66. Detailed flux variation with PVC (Vs).
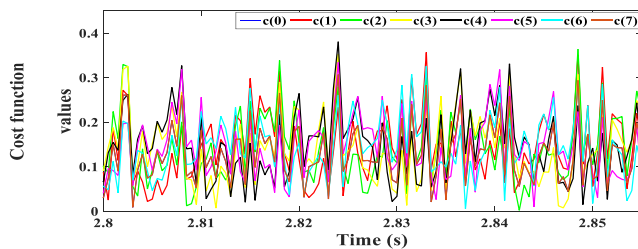
FIGURE 67. Detailed view of cost function's values with PVC.
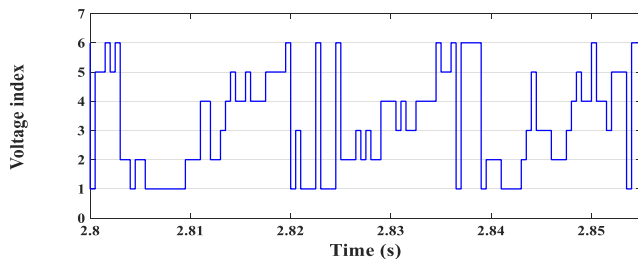
FIGURE 68. Detailed view of selected voltage index with PVC.

The performed commutations is also compared for the two procedures, and the statistics are addressed in Table 2. It can be noticed that the performed commutations under the PVC are much lower than that of MP DTC, which effectively helps in restricting the switching losses under the PVC approach. This fact can be easily explained by checking the cost functions of the two procedures. For the MP DTC, and to evaluate the cost function in (28), the torque and flux must be firstly calculated which consumes much time. On the other hand, in PVC, the cost function of (27) does not contain any term needs to be evaluated and thus the time taken for computation is much lower.

VII. EXPERIMENTAL VALIDATION
To verify the effectivity of the formulated sensorless PVC approach, the experimental tests are executed under the same operating conditions given in Sec. VI. The experimental layout is shown in Figure 42, which consists mainly of three
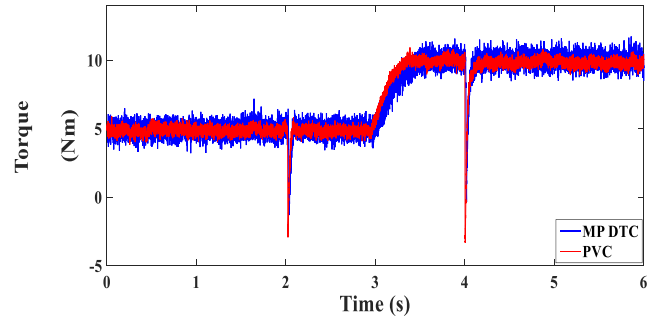

FIGURE 69. Torque dynamics for the two approaches (Nm).
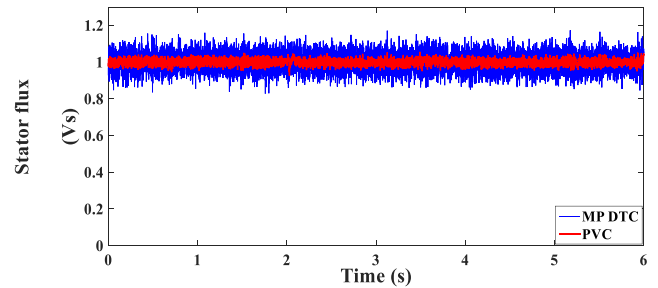
FIGURE 70. Flux dynamics for the two approaches (Vs).

sections: the power section, the control section and instrumentation section. A three-phase wound rotor type IM is used in which the rotor terminals are short circuited, and the stator's terminals are connected to the inverter's terminals. The inverter is also connected to the dSPACE connector panel (CP 1104) via two data cables. The voltages and currents are sensed using Hall Effect sensors which are connected to the CP 1104 which is responsible for delivering the analogue signals to the PC using Analogue/Digital (A/D) converters. The sampled and measured variables are then entered to the dSPACE 1104 control desk environment installed on the PC.

A. PERFORMANCE OF MP DTC WITH BSO
The dynamics of MP DTC are tested experimentally for a change in the rotational speed of $800 \rightarrow 400 \rightarrow 20$ RPM at times t = 0s, t = 2 s and t = 4 s. The flux reference is set to 1 Vs. The torque reference is obtained using a PI speed regulator. The motor is loaded at starting with 5 Nm and then at time t = 3 s, the torque is raised to the 10 Nm (nominal torque). A variation in the rotor and stator resistances is made at times t = 2.5 s and t = 3.5 s, so that their values become 1.5 times of their actual ones. The BSO is used to provide the estimated flux, current, speed and stator and rotor resistances. The reference voltages components are obtained using the designed flux and torque regulators.

Figures 43, 44 and 45 show the speed, torque and stator flux profiles of IM under MP DTC. From Figure 43, it is noticed that the proposed BSO succeeded in estimating the speed with high matching degree. In Figure 44, the developed torque show a change at t = 3 s as a respond to the torque reference; however remarkable torque ripples are noticed. In Figure 45,

FIGURE 71. Flux loci for the two approaches.

FIGURE 72. α-component current with MP DTC (A).

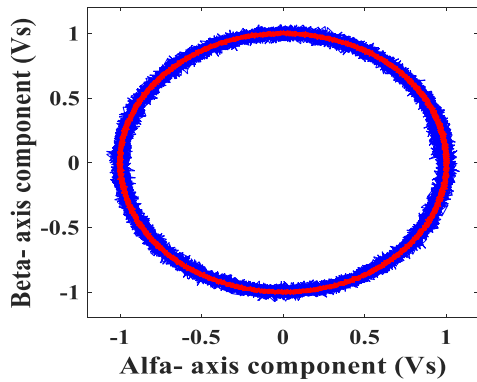the flux is following precisely the flux reference but with noticeable oscillations. The observed α-β signals of stator current and rotor flux and their observation errors are shown respectively in Figures 46 and 47.

The estimated and actual quantities of stator and rotor resistances are shown in Figures 48 and 49. These figures prove the effectivity of the BSO in tracking the parameters change which as a result improves the system's robustness.

The robustness of the sensorless scheme is also approved via checking the profiles of the real and observed position and the resultant estimation error shown respectively in Figures 50 and 51. A concentrated view for the MP DTC dynamics is presented in Figures 52, 53, 54 and 55 which show a sample torque variation, a sample flux variation, calculated cost function and voltage index variation. From these figures, it is very obvious that according to the values of cost function, the voltage index changes its state in the way that the voltage which minimizes the error is selected.

B. PERFORMANCE OF PROPOSED PVC WITH BSO

The IM dynamics are tested experimentally for the same operating regimes introduced for the MP DTC. Figures 56, 57 and 58 illustrate the estimated and actual speed, the developed torque and estimated stator flux. The speed profile proves the validity of the proposed BSO in achieving a precise tracking of the actual speed, meanwhile the calculated values of torque and flux exhibit much lower ripples in relative to the calculated values under MP DTC. The estimated and actual values of the stator current and rotor flux components and the related estimation errors are shown in Figures 59 and 60, respectively. From the estimation error profiles, it can be noticed that the BSO successfully achieved its target by maintaining a very small deviation between the real and observed variables.

The estimation of stator and rotor resistances is also accomplished using the BSO as shown in Figures 61 and 62, respectively. The precise track of estimated resistances to
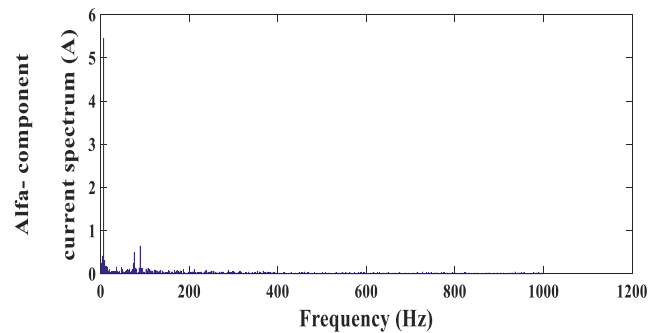
FIGURE 73. α-component current spectrum with MP DTC.

FIGURE 74. β-component current with MP DTC (A).

FIGURE 75. β-component current spectrum with MP DTC.

their actual values are achieved which contributed effectively in enhancing the system's robustness. Figures 63 and 64 illustrate the estimated and actual positions and the

FIGURE 76. α-component current with PVC (A).
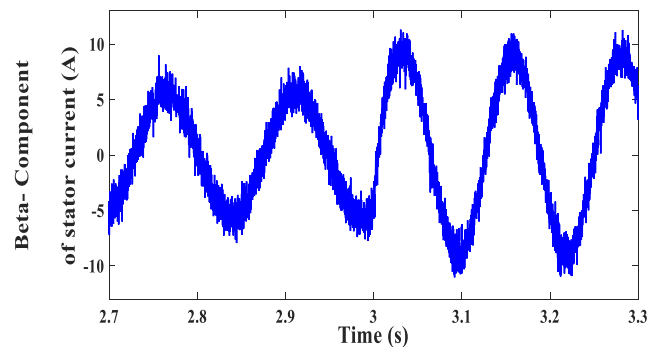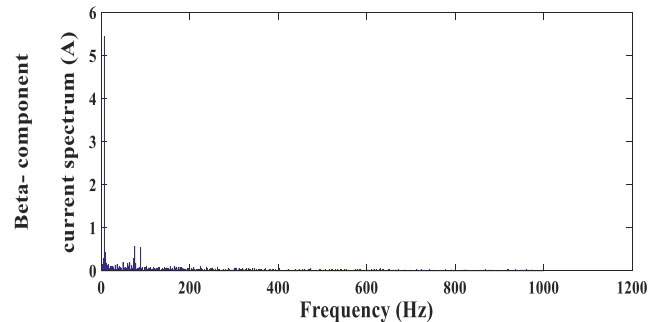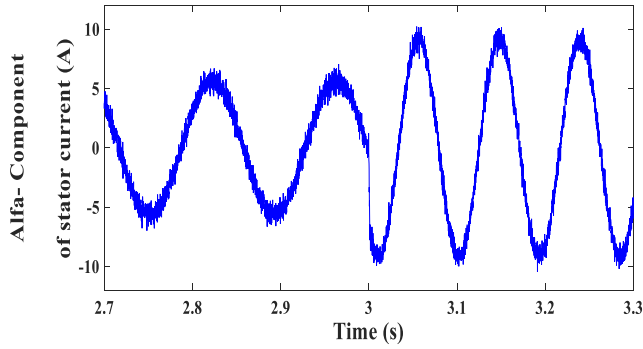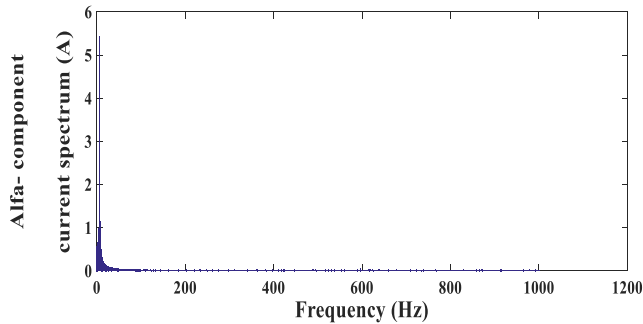

FIGURE 77. α-component current spectrum with PVC.

FIGURE 78. β-component current with PVC (A).

FIGURE 79. β-component current spectrum with PVC.

TABLE 3. Currents spectrums under MP DTC and PVC approaches (experimental).

Algorithm	current spectrums	
	$i_{\alpha s}$	$i_{\beta s}$
MP DTC	Fundamental (5.44529A) THD= 4.67 %	Fundamental (5.43975A) THD= 4.29 %
PVC	Fundamental (5.43345A) THD= 1.17 %	Fundamental (5.21659 A) THD= 1.22 %

TABLE 4. Number of commutations for both techniques.

Technique	Commutations	Switching frequency
MP DTC	12127	2.017 KHz
Proposed PVC	6486	1.081 KHz

MP DTC. The comparison is also made through analyzing the FFT spectrums for the stator current's α-β components as shown in Figs 73 and 75 for the MP DTC and in Figs 77 and 79 for the proposed PVC. By checking, it is found that the currents under PVC exhibit less harmonics. The values of THD are presented in Table 3.

The comparison in terms of number of commutations is also carried out between the two control procedures. The statistics are recorded in Table 4 through which it can be realized that the proposed PVC has succedded in limiting the number of commutations thanks to the simple form of proposed cost function given in (27).

VIII. CONCLUSION

The paper introduced a novel predictive voltage control (PVC) for a sensorless IM drive using a robust back-stepping observer (BSO). The design procedures for the proposed PVC and BSO are introduced and described in details. The operation principle of the PVC is established on regulating the deviation of the applied voltage from its reference signal, and thus the used cost function is free of the estimated variables which simplifies the system's structure. The proposed BSO considers the observation of stator and rotor resistances to enhance the stability of the system versus the parameters variation. To approve the validity of the

related error. From these figures, the validity of the BSO is ensured through obtaining minimum estimation error. A detailed control action is illustrated in Figures 65, 66, 67 and 68 which show the torque variation, flux variation, calculated values of cost function and stator voltage index, respectively. Compared with Figures 52 and 53 obtained under MP DTC, the torque and flux deviations in Figures 65 and 66 are much lower which confirm the superiority of proposed PVC over the MP DTC approach.

In order to illustrate the improved dynamic behavior of IM drive under PVC, the profiles of flux, torque and iso flux are presented for the two procedures as shown in Figs 69, 70 and 71. Through these figures, it is easy to realize that the proposed PVC has better dynamics than the
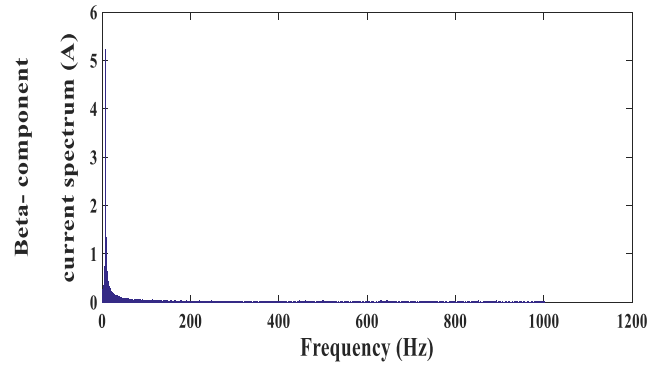
designed PVC, a detailed comparison is carried out between the traditional MP DTC and the proposed PVC. The comparison tests are performed by simulation using Matlab software and experimentally using a dSPACE 1104 control board. The obtained results confirm the validness of the presented PVC in achieving better dynamics than the MP DTC in terms of ripples content, simplicity, number of commutations and switching frequency.

APPENDIX

TABLE 5. Parameters of IM Drive.

Parameters	Value	Parameters	Value
Rated power	3 Kw	σ	0.07576 H
R_s	1.50 Ω	K_p, $K_{I\,(Speed\,Controller)}$	14.24 and 1267
R_r	0.85 Ω	K_p, $K_{I\,(Torque\,Controller)}$	80 and 230
L_s	0.1785 H	K_p, $K_{I\,(Flux\,Controller)}$	7000 and 20000
L_r	0.18451 H	p (pole pairs)	1
L_m	0.17447 H	U_{dc}	300 V

REFERENCES

[1] Y. Zhang and H. Yang, "Model predictive torque control of induction motor drives with optimal duty cycle control," *IEEE Trans. Power Electron.*, vol. 29, no. 12, pp. 6593–6603, Dec. 2014.

[2] F. Wang, S. Li, X. Mei, W. Xie, J. Rodriguez, and R. M. Kennel, "Model-based predictive direct control strategies for electrical drives: An experimental evaluation of PTC and PCC methods," *IEEE Trans. Ind. Informat.*, vol. 11, no. 3, pp. 671–681, Jun. 2015.

[3] X.-H. Jin, Y. Zhang, and D.-G. Xu, "Static current error elimination algorithm for induction motor predictive current control," *IEEE Access*, vol. 5, pp. 15250–15259, 2017.

[4] M. A. Mossa and S. Bolognani, "Robust predictive current control for a sensorless IM drive based on torque angle regulation," in *Proc. IEEE Conf. Power Electron. Renew. Energy (CPERE)*, Aswan City, Egypt, Oct. 2019, pp. 302–308.

[5] Y. Zhang, H. Yang, and B. Xia, "Model-predictive control of induction motor drives: Torque control versus flux control," *IEEE Trans. Ind. Appl.*, vol. 52, no. 5, pp. 4050–4060, Sep. 2016.

[6] M. A. Abbasi, A. R. Husain, N. R. N. Idris, W. Anjum, H. Bassi, and M. J. H. Rawa, "Predictive flux control for induction motor drives with modified disturbance observer for improved transient response," *IEEE Access*, vol. 8, pp. 112484–112495, 2020.

[7] Y. Zhang, B. Xia, H. Yang, and J. Rodriguez, "Overview of model predictive control for induction motor drives," *Chin. J. Electr. Eng.*, vol. 2, no. 1, pp. 62–76, Jun. 2016.

[8] Y. Cho, Y. Bak, and K.-B. Lee, "Torque-ripple reduction and fast torque response strategy for predictive torque control of induction motors," *IEEE Trans. Power Electron.*, vol. 33, no. 3, pp. 2458–2470, Mar. 2018.

[9] Y. Zhang, H. Yang, and B. Xia, "Model predictive torque control of induction motor drives with reduced torque ripple," *IET Electr. Power Appl.*, vol. 9, no. 9, pp. 595–604, Nov. 2015.

[10] J. Wang, F. Wang, G. Wang, S. Li, and L. Yu, "Generalized proportional integral observer based robust finite control set predictive current control for induction motor systems with time-varying disturbances," *IEEE Trans. Ind. Informat.*, vol. 14, no. 9, pp. 4159–4168, Sep. 2018.

[11] S. Vazquez, J. Rodriguez, M. Rivera, L. G. Franquelo, and M. Norambuena, "Model predictive control for power converters and drives: Advances and trends," *IEEE Trans. Ind. Electron.*, vol. 64, no. 2, pp. 935–947, Feb. 2017.

[12] H. Guzman, F. Barrero, and M. J. Duran, "IGBT-gating failure effect on a fault-tolerant predictive current-controlled five-phase induction motor drive," *IEEE Trans. Ind. Electron.*, vol. 62, no. 1, pp. 15–20, Jan. 2015.

[13] W. Xu, J. Zou, Y. Liu, and J. Zhu, "Weighting factorless model predictive thrust control for linear induction machine," *IEEE Trans. Power Electron.*, vol. 34, no. 10, pp. 9916–9928, Oct. 2019.

[14] M. Uddin, S. Mekhilef, M. Rivera, and J. Rodriguez, "Predictive indirect matrix converter fed torque ripple minimization with weighting factor optimization," in *Proc. Int. Power Electron. Conf. (IPEC-Hiroshima-ECCE ASIA)*, Hiroshima, Japan, May 2014, pp. 3574–3581.

[15] S. A. Davari, V. Nekoukar, C. Garcia, and J. Rodriguez, "Online weighting factor optimization by simplified simulated annealing for finite set predictive control," *IEEE Trans. Ind. Informat.*, vol. 17, no. 1, pp. 31–40, Jan. 2021.

[16] L. Yan, M. Dou, H. Zhang, and Z. Hua, "Speed-sensorless dual reference frame predictive torque control for induction machines," *IEEE Trans. Power Electron.*, vol. 34, no. 12, pp. 12285–12295, Dec. 2019.

[17] L.-J. Cheng and M.-C. Tsai, "Enhanced model predictive direct torque control applied to IPM motor with online parameter adaptation," *IEEE Access*, vol. 8, pp. 42185–42199, 2020.

[18] Y. Zhang and H. Yang, "Model-predictive flux control of induction motor drives with switching instant optimization," *IEEE Trans. Energy Convers.*, vol. 30, no. 3, pp. 1113–1122, Sep. 2015.

[19] T. Orlowska-Kowalska, "Application of extended Luenberger observer for flux and rotor time-constant estimation in induction motor drives," *IEE Proc. D Control Theory Appl.*, vol. 136, no. 6, pp. 324–330, Nov. 1989.

[20] B. Karanayil, M. F. Rahman, and C. Grantham, "Implementation of an on-line resistance estimation using artificial neural networks for vector controlled induction motor drive," in *Proc. 29th Annu. Conf. IEEE Ind. Electron. Soc. (IECON)*, vol. 2, Nov. 2003, pp. 1703–1708.

[21] M. Cirrincione, M. Pucci, G. Cirrincione, and G.-A. Capolino, "A new experimental application of least-squares techniques for the estimation of the induction motor parameters," *IEEE Trans. Ind. Appl.*, vol. 39, no. 5, pp. 1247–1256, Sep. 2003.

[22] R. Marino, S. Peresada, and P. Tomei, "On-line stator and rotor resistance estimation for induction motors," *IEEE Trans. Control Syst. Technol.*, vol. 8, no. 3, pp. 570–579, May 2000.

[23] K. Ohyama, G. M. Asher, and M. Sumner, "Comparative analysis of experimental performance and stability of sensorless induction motor drives," *IEEE Trans. Ind. Electron.*, vol. 53, no. 1, pp. 178–186, Feb. 2006.

[24] H. M. Kojabadi, L. Chang, and R. Doraiswami, "A MRAS-based adaptive pseudoreduced-order flux observer for sensorless induction motor drives," *IEEE Trans. Power Electron.*, vol. 20, no. 4, pp. 930–938, Jul. 2005.

[25] M. H. Holakooie, M. Ojaghi, and A. Taheri, "Modified DTC of a six-phase induction motor with a second-order sliding-mode MRAS-based speed estimator," *IEEE Trans. Power Electron.*, vol. 34, no. 1, pp. 600–611, Jan. 2019.

[26] T.-S. Kwon, M.-H. Shin, and D.-S. Hyun, "Speed sensorless stator flux-oriented control of induction motor in the field weakening region using luenberger observer," *IEEE Trans. Power Electron.*, vol. 20, no. 4, pp. 864–869, Jul. 2005.

[27] S. M. J. Rastegar Fatemi, N. R. Abjadi, J. Soltani, and S. Abazari, "Speed sensorless control of a six-phase induction motor drive using backstepping control," *IET Power Electron.*, vol. 7, no. 1, pp. 114–123, Jan. 2014.

[28] J. Talla, V. Q. Leu, V. Smidl, and Z. Peroutka, "Adaptive speed control of induction motor drive with inaccurate model," *IEEE Trans. Ind. Electron.*, vol. 65, no. 11, pp. 8532–8542, Nov. 2018.

[29] M. Morawiec, P. Strankowski, A. Lewicki, J. Guzinski, and F. Wilczynski, "Feedback control of multiphase induction machines with backstepping technique," *IEEE Trans. Ind. Electron.*, vol. 67, no. 6, pp. 4305–4314, Jun. 2020.

[30] S. Drid, M.-S. Naït-Saïd, and M. Tadjine, "Robust backstepping vector control for the doubly fed induction motor," *IET Control Theory Appl.*, vol. 1, no. 4, pp. 861–868, Jul. 2007.

[31] M. S. Alam and M. R. Khan, "Stability analysis of a five-phase induction motor drive using variable frequency technique," *Universal J. Electr. Electron. Eng.*, vol. 4, no. 5, pp. 120–128, Oct. 2016.

[32] J. Chen and J. Huang, "Stable simultaneous stator and rotor resistances identification for speed sensorless IM drives: Review and new results," *IEEE Trans. Power Electron.*, vol. 33, no. 10, pp. 8695–8709, Oct. 2018.

MAHMOUD A. MOSSA received the bachelor's and master's degrees in electrical engineering from the Faculty of Engineering, Minia University, Egypt, in 2008 and 2013, respectively, and the Ph.D. degree in electrical energy engineering from the University of Padova, Italy, in April 2018. Since January 2010, he has been working as an Assistant Lecturer with the Electrical Engineering Department, Minia University. In November 2014, he joined the Electric Drives Laboratory (EDLAB), University of Padova, for his Ph.D. research activities. Since May 2018, he has been working as an Assistant Professor with the Electrical Engineering Department, Minia University. His research interests include electric machine drives, power electronics, renewable energy systems, and load frequency control.

HAMDI ECHEIKH was born in Tozeur, Tunisia, in 1988. He received the Electrical Engineer Diploma and master's degrees from the National Engineering School of Monastir (ENIM), Tunisia, in 2011 and 2013, respectively, and the Ph.D. degree in electrical engineering from the National Engineering School of Monastir. His research interests include multiphase machine drives, renewable energies, power electronics, linear and nonlinear control systems, and design of observers applied for electrical machines.

NGUYEN VU QUYNH was born in Vietnam, in 1979. He received the B.S. and M.S. degrees in electrical engineering from the Ho Chi Minh City University of Technology and Education, Vietnam, in 2003 and 2005, respectively, and the Ph.D. degree in electrical engineering from the Southern Taiwan University of Science and Technology, Tainan, Taiwan, in 2013. He is currently the Vice President of Lac Hong University, Vietnam. His research interests include advanced control techniques, electric machine drives, renewable energy conversion, and robots.

● ● ●